

Electronic Supplementary Information

Glutathione activation of an organometallic half-sandwich anticancer drug candidate by ligand attack

Xin Zhang, ^{a†} Fortuna Ponte, ^{b†} Elisa Borfecchia, ^c Andrea Martini, ^c Carlos Sanchez-Cano, ^{a,d*} Emilia Sicilia, ^{b*} and Peter J. Sadler ^{a*}

^{a.} *Department of Chemistry, University of Warwick, Coventry, CV4 7AL, UK*

E-mail: p.j.sadler@warwick.ac.uk

^{b.} *Dipartimento di Chimica e Tecnologie Chimiche, Università della Calabria, Ponte P. Bucci, Cubo 14cl-87030, Arcavacata di Rende, Italy*

E-mail: emilia.sicilia@unical.it

^{c.} *Department of Chemistry and INSTM Reference Center, University of Turin, via Giuria 7, 10125, Turin, Italy*

^{d.} Current address: *CIC biomaGUNE, Parque Científico y Tecnológico de Gipuzkoa, Paseo Miramón 182, 20014 San Sebastian, Spain*

E-mail: csanchez@cicbiomagune.es

† These authors contributed equally to the manuscript.

Table of Contents

Synthesis and characterisation of hydrolysis products	S3
Experimental validation of DFT geometries by EXAFS and simulation of the 1-GS/NN intermediate	S4
Materials	S7
Methods	S9
Tables	S18
Table S1 LC/MS and HRMS identifications for osmium species	S18
Table S2 Extinction coefficients of osmium complexes	S18
Table S3-S6 HPLC studies for reactions of osmium complexes with thiols	S19
Table S7-S9 XAS simulations for the reactions of 1-I with GSH	S21
Table S10 ¹ H NMR studies for the reactions of 1-I with GSH	S23
Figures	S24
Fig. S1-S3 DFT calculations for osmium complexes with GSH	S24
Fig. S4-S14 HRMS for osmium species	S27
Fig. S15 pK _a of 1-OH	S32
Fig. S16 UV-Vis spectra for aqueous solutions of osmium complexes	S33
Fig. S17-S27 HPLC studies for reactions of osmium complexes with thiols	S33
Fig. S28-S39 XAS studies for reactions of 1-I with GSH	S39
Fig. S40 Studies of catalytic nature of the reaction of 1-I with GSH	S49
References	S51

Synthesis and characterisation of hydrolysis products

Both osmium hydroxido (**1-OH**), and osmium thiolate species (**1-SG** and **1-NAC**) are observed when **1-I** reacts with thiols such as GSH or N-acetyl-L-cysteine (NAC),¹ but they had not been previously isolated. Here we used a synthetic procedure (Materials Section Page S6) which provides **1-OH**, **1-SG** and **1-NAC** in good yield (**Chart S1**) with full characterisation (Materials Section Page S7, Table S1, Fig. S4-S14). In general, **1-OH** was prepared by removing chloride ligands (using AgNO₃) from the dimer precursor, which was reacted then with the azopyridine ligand. This generated complex **1-NO₃•PF₆**, which could be easily isolated, and hydrolysed to **1-OH** in aqueous solution. Thiolate adducts **1-SG** and **1-NAC**, on the contrary, were prepared by reacting **1-Cl** with excess of the required thiols under basic conditions in an N₂ atmosphere.

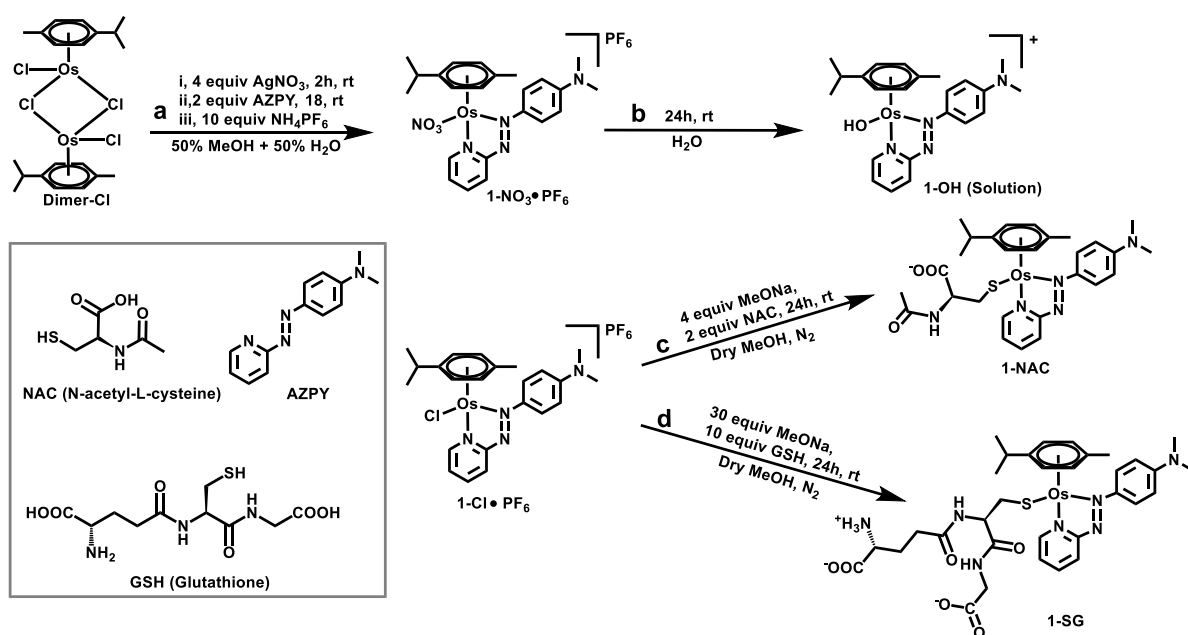


Chart S1. Structures of organo-osmium complexes studied here and synthetic routes.

The pK_a value of **1-OH₂** was determined by ¹H NMR methods (pK_a = 5.20 ± 0.02; Fig. S15), confirming the hydroxido nature of **1-OH** at physiological pH. Furthermore, by combining UV-Vis spectroscopy of the adducts observed in the reaction between **1-I**

and thiols (i.e. **1-CI**, **1-I**, **1-OH**, **1-SG** or **1-NAC**; Fig. S16), with ICP-OES analysis, extinction coefficients at 610 nm were determined (Table S2). We used these extinction coefficients to quantify the different Os species generated during the hydrolysis of **1-I** based on the proportionality between HPLC peak areas at 610 nm and the known concentration of those osmium complexes (Fig. S17). This allowed the kinetics of the reactions to be studied by HPLC.

Experimental validation of DFT geometries by EXAFS and simulation of the 1-GS/NN intermediate

Fourier-transformed EXAFS data allowed obtaining direct information on the characteristic scattering contributions stemming from the atoms in the proximity of Os centres of the different complexes (**1-I**, **1-CI**, **1-OH** and **1-SG**; Fig. 2c,d main text, Fig. S30). From this, we determined that the low-R ranges of the spectra of **1-I**, **1-CI** and **1-SG** (up to ≈ 1.8 Å in the phase-uncorrected spectra) were mainly dominated by contributions from low-Z scatterers (N atoms from pyridylazo ligand and C atoms from *p*-cym), resulting in a similar EXAFS signal. **1-OH** was instead characterised by a pronounced enhancement of the EXAFS signal in the low-R range with respect to the other complexes. This was consistent with the presence of an Os–O single scattering (SS) contribution in addition to contributions from pyridylazolate N and *p*-cym C atoms. At higher distances from the Os centre, we observed a prominent peak for **1-I**, centred at ≈ 2.5 Å, arising from the Os–I single SS. Smaller features at ≈ 2.0 Å due to the presence of S or Cl atoms in the first coordination sphere of **1-SG/1-CI** complexes were also observed. Finally, the exclusive presence of low-Z scatterers in **1-OH** was also marked by the distinct shape of the FT-EXAFS signal.

We used this information to validate the structural models from DFT against the available experimental EXAFS spectra. Initially, the computational models of **1-I** and **1-SG** were used as the starting hypothesis to fit EXAFS spectra collected from solid-

state standards, and results were assessed according to the quality and physical reliability of the optimised values of the structural parameters obtained. The best-fit curves shown in Fig. S31 illustrate the quality of our fits, as they adequately reproduced all the experimental features in the R-space range considered in our analysis, resulting in fit R-factors < 2% (Table S7). Furthermore, the optimised bond distances obtained were in substantial agreement with the x-ray crystal structure of **1-I** and the DFT models for both complexes. However, EXAFS analysis revealed a slight elongation of the average Os–N₁ bond length (up to 0.03 Å) paralleled by a slight contraction of the average Os–C₁ distance (up to 0.08 Å) with respect to theoretical predictions. Moreover, the Os–I distance in **1-I** was optimised at (2.708 ± 0.004) Å (in good agreement with x-ray crystal structure), whereas the S ligand in **1-SG** was refined at (2.39 ± 0.01) Å (corroborating the qualitative interpretation of the R-ranges between 2-2.5 Å of the FT-EXAFS proposed above). Again, contractions in the order of 0.06 Å were noted in both cases with respect to the respective DFT models. Nevertheless, all the other fitting parameters were optimised to physically reliable values, falling in their respective expectation intervals under the relevant experimental conditions. Finally, Debye-Waller (DW) factors for the N₁ and C₁ shells were higher for **1-SG** ($\sigma_{2N1} = 0.0024 \pm 0.0006 \text{ \AA}^2$; $\sigma_{2C1} = 0.004 \pm 0.001 \text{ \AA}^2$) with respect to **1-I** ($\sigma_{2N1} = 0.0011 \pm 0.0008 \text{ \AA}^2$; $\sigma_{2C1} = 0.0015 \pm 0.0008 \text{ \AA}^2$), suggesting a higher degree of structural disorder for the former adduct.

Once the DFT models were validated, we used them to obtain valuable structural information from the EXAFS spectra acquired from **1-I** standards in three different aqueous environments (pH = 3, 5 and 7; Table S8, Fig. S32). This was important as those were the main conditions used during our XAS experiments to study the hydrolysis of **1-I** in presence of GSH. Data analysis indicated that, when **1-I** is in solution, the closest Os coordination environment is substantially similar to the solid-state configuration, and adequately predicted by the DFT model (fit R-factor < 3% in all cases). This is particularly true at pH 5 and 7, where the all optimised values

obtained for structural parameters are equivalent with those found from the solid-state standards. However, at pH 3 we observed a slight contraction of the Os–N₁ bond length ($2.02 \pm 0.01 \text{ \AA}$ vs $2.06 \pm 0.03 \text{ \AA}$ for the solid-state standard). EXAFS also showed evidence for a higher degree of structural disorder for **1-I** standards in solution, reflected by a global increase in DWs and fitting uncertainties with respect to the solid-state standards (Table S7). However, a remarkably good fitting quality is still attained.

Taken together, these fitting results highlighted the validity of the computational approach adopted, and provided experimentally-validated values for structural (average deviations from DFT bond distances) and spectroscopic (e.g. passive scattering amplitude, energy shift, and DW factors) parameters for the Os-complexes relevant to our study. Based on these results, we were able to simulate the EXAFS signature corresponding to the DFT model of **1-GS/NN** (structure in Fig. S31e-f). Interestingly, the signal simulated for **1-GS/NN** only shows small shifts to lower distances and a minor intensity enhancement at low-ranges R when compared to the experimental spectra of both **1-I** and **1-SG**. Conversely, from 1.8 \AA upward, the absence of scattering contribution from close high-Z atomic neighbours (in this case, S falls at $\approx 4.5 \text{ \AA}$ from the Os centre), results into a distinct, unstructured, EXAFS signal. Such differences can also be clearly observed in the contrast in k-space EXAFS oscillations between the experimental spectra of **1-I** and **1-SG** and the simulated spectrum of the synthetically inaccessible intermediate (Fig. S31g). More importantly, our calculations based on experimentally-validated models allowed attempts to probe the presence of **1-GS/NN** when the reaction between **1-I** and GSH was followed *in situ* by EXAFS.

Materials

Osmium dimers ($[\text{Os}(\eta^6\text{-}p\text{-cym})\text{X}_2]_2$, where X = Cl or I), $[\text{Os}(\eta^6\text{-}p\text{-cymene})(4\text{-}(2\text{-pyridylazo})\text{-}N,N\text{-dimethylaniline})\text{I}]\text{PF}_6$ (**1-I•PF₆**), $[\text{Os}(\eta^6\text{-}p\text{-cymene})(4\text{-}(2\text{-pyridylazo})\text{-}N,N\text{-dimethylaniline})\text{Cl}]\text{PF}_6$ (**1-Cl•PF₆**), $[\text{Os}(\eta^6\text{-}p\text{-cymene})(4\text{-}(2\text{-iminopyridine})\text{-}N,N\text{-dimethylaniline})\text{Cl}]\text{PF}_6$ (**1-impy-Cl•PF₆**) and $[\text{Os}(\eta^6\text{-}p\text{-cymene})(4\text{-}(2\text{-iminopyridine})\text{-}N,N\text{-dimethylaniline})\text{I}]\text{PF}_6$ (**1-impy-I•PF₆**) were prepared by previously reported procedures.²⁻⁴ Reduced glutathione (**GSH**), N-acetyl-L-cysteine (**NAC**), silver nitrate, 1,4-dithiothreitol (**DTT**) were purchased from Sigma Aldrich. Pyridine-2-azo-p-dimethylaniline was purchased from Alfa Aesar. Sodium hydroxide, sodium chloride, sodium phosphate dibasic, sodium phosphate monobasic, trifluoroacetic acid were purchased from Fisher Scientific. All other solvents and reagents for synthesis and analysis were purchased from commercial suppliers and used as received.

Synthesis of $[\text{Os}(\eta^6\text{-}p\text{-cymene})(4\text{-}(2\text{-pyridylazo})\text{-}N,N\text{-dimethylaniline})\text{NO}_3]\text{PF}_6$ (1-NO₃•PF₆**) & $[\text{Os}(\eta^6\text{-}p\text{-cymene})(4\text{-}(2\text{-pyridylazo})\text{-}N,N\text{-dimethylaniline})\text{OH}]^+$ (**1-OH**).** To a stirred solution of $[\text{Os}(\eta^6\text{-}p\text{-cymene})\text{Cl}_2]_2$ (158 mg, 0.2 mmol) in methanol (10 mL), AgNO_3 (136 mg, 0.8 mmol) in water (10 mL) was added. Then the solution was stirred 310 K for 2 h and generated a white precipitate which was removed by filtration. Then a solution of pyridine-2-azo-p-dimethylaniline (90.4 mg, 0.4 mmol) in methanol (5 mL) was added. The mixture was stirred for 18 h at ambient temperature. The volume of the solution was reduced to ca. 2 mL under reduced pressure and then ammonium hexafluorophosphate (326 mg, 2 mmol) was added, using ultrasonic to promote dissolution. The solution was left in a freezer (ca. 268 K) overnight and a deep-blue precipitate was collected *via* vacuum filtration, washed with ice-cold ethanol (2×1 mL), diethyl ether (2 × 5 mL), and then dried overnight in a vacuum desiccator. Yield: 96 mg (40%). From HRMS, ¹H NMR and C H N analysis, the product was **1-NO₃•PF₆**. HRMS calculated for $[\text{1-NO}_3]^+$ ($\text{C}_{23}\text{H}_{28}\text{N}_5\text{O}_3\text{Os}^+$) m/z 614.1802, found: 614.1809. ¹H NMR (CD_3OD) with 400 MHz: δ = 9.45 (d, 1H, J = 5.2 Hz), 8.39 (d, 1H, J = 8.0 Hz), 8.30-8.24 (m, 3H), 7.60 (t, 1H, J = 7.1 Hz), 7.03 (d, 2H,

J = 9.5 Hz), 6.59 (d, 1H, J = 5.9 Hz), 6.35 (d, 1H, J = 5.8 Hz), 6.20-6.00 (m, 2H), 3.43 (s, 6H), 2.39 (s, 3H), 2.30-2.20 (m, 1H), 0.95-0.82 (dd, 6H, J = 6.9 Hz). CHN analysis: calculated for C₂₃H₂₈F₆N₅O₃OsP (**1-NO₃•PF₆**): C, 36.46%; H, 3.72%; N, 9.24%. Found: C, 36.52%; H, 3.69%; N, 9.17%.

1-NO₃•PF₆ was dissolved into water and stirred for 24 h at ambient temperature, giving [**1-OH**]⁺ solution with NO₃⁻. HRMS calculated for [**1-OH**]⁺ (C₂₃H₂₉N₄OOs⁺): m/z 569.1951. Found: 569.1941. ¹H NMR(D₂O) with 400 MHz: δ = 9.23 (d, 1H, J = 5.7 Hz), 8.35 (d, 1H, J = 8.4 Hz), 8.14-8.21 (m, 3H), 7.60 (t, 1H, J = 6.6 Hz), 6.99 (d, 2H, J = 9.5 Hz), 6.38 (d, 1H, J = 5.7 Hz), 6.18-6.24 (m, 2H), 6.14 (d, 1H, J = 5.6 Hz), 3.39 (s, 6H), 2.35 (s, 3H), 2.20-2.12 (m, 1H), 0.85-0.70 (dd, 6H, J = 6.9 Hz).

Synthesis of Os(η⁶-*p*-cymene)(4-(2-pyridylazo)-*N,N*-dimethylaniline)N-acetyl-L-cysteine (1-NAC**).** [Os(η⁶-*p*-cymene)(4-(2-pyridylazo)-*N,N*-dimethylaniline)Cl]PF₆ (**1-Cl•PF₆**) (146.2 mg, 0.2 mmol), MeONa (43.2 mg, 0.8 mmol) and N-acetyl-L-cysteine (65.2 mg, 0.4 mmol) were placed in a 25 mL flask. The air in the flask was displaced by N₂. Dry methanol (10 mL) was injected into the flask and the solution was stirred at ambient temperature for 24 h with the protection of N₂. Then the reaction mixture was filtered and the solvent was removed under reduced pressure. Flash chromatography was used to purify the product, and a deep-blue powder was obtained which was dried in a vacuum desiccator. Yield 86.67 mg (50.9%). HRMS calculated for [**1-NAC + H**]⁺ (C₂₈H₃₆N₅O₃SOs⁺): m/z 714.2147. Found: 714.2149. ¹H NMR (CD₃OD) with 400 MHz: δ = 9.15 (d, 1H, J = 5.7 Hz), 8.50 (d, 1H, J = 8.1 Hz), 8.12-7.94 (m, 3H), 7.5 (t, 1H, J = 6.6 Hz), 6.88 (d, 2H, J = 8.3 Hz), 6.33-6.29 (dd, 1H, J = 5.8 Hz), 6.10-6.04 (dd, 1H, J = 7.8 Hz), 5.90-5.82 (m, 2H), 4.02-3.95 (m, 1H), 3.28 (s, 6H), 2.49 (d, 3H, 5.6), 2.32-2.22 (m, 1H), 2.03-1.70 (m, 5H), 0.81-0.75 (m, 6H). CHN analysis: calculated for C₂₉H₄₀ClN₅Na₂O₅OsS (**1-NAC + CH₃OH + NaCl + NaOH**): C, 41.17%; H, 4.72%; N, 8.20. Found: C, 41.31%; H, 4.65%; N, 8.28.

Synthesis of Os(η^6 -*p*-cymene)(4-(2-pyridylazo)-*N,N*-dimethylaniline)glutathione (1-SG). [Os(η^6 -*p*-cymene)(4-(2-pyridylazo)-*N,N*-dimethylaniline)Cl]PF₆ (1-Cl•PF₆) (146.2 mg, 0.2 mmol), MeONa (324 mg, 6 mmol) and glutathione (γ -L-Glu-L-Cys-Gly) (614.4 mg, 2 mmol) were placed to a 25 mL flask. The air in the flask was displaced by N₂. Dry methanol (10 mL) was injected into the flask and the solution was stirred at ambient temperature for 24 h under N₂. Then the reaction mixture was filtrated and the solvent was removed under reduced pressure. Flash chromatography was used to purify the product, giving a deep-blue powder was dried in a vacuum desiccator. Yield 106.56 mg (53.28%). HRMS calculated for [1-SG + H⁺] (C₃₃H₄₄N₇O₆OsS⁺): m/z 858.2682. Found: 858.2693. ¹H NMR (CD₃OD): δ = 9.20 (dd, 1H, J = 5.3 Hz), 8.52 (d, 1H, J = 8.9 Hz), 8.13-8.05 (m, 3H), 7.54 (t, 1H, 6.3 Hz), 6.94-6.88 (m, 2H), 6.29-6.26 (m, 1H), 6.05-6.03 (m, 1H), 5.90-5.86 (m, 2H), 3.85-3.50 (m, 4H), 3.36 (s, 2H), 3.31 (s, 6H), 2.46 (d, 3H, J = 3.6 Hz), 2.40-2.17 (m, 3H), 2.15-1.49 (m, 5H), 0.82-0.68 (m, 6H). CHN analysis: calculated for C₃₄H₄₄Cl₂N₇NaO₆OsS (1-SG - H⁺ + Na⁺ + CH₂Cl₂): C, 42.41%; H, 4.61%; N, 10.18%. Found: C, 42.36%; H, 4.67%; N, 10.23%.

Methods

Flash chromatography. Complexes were purified using a Biotage Isolera One instrument with a Biotage® KP-Sil 10g SNAP cartridge. The mobile phase consisted of: (A) dichloromethane, and (B) methanol. The crude products with ISOLUTE HM-N granules were installed onto the top of the column. The following solvent gradient was used with a 12 mL/min flow rate.

Start % (B)	End % (B)	Column volume
0	0	10
0	10	20
10	50	20-50
50	50	20
50	0	10

The collected fractions were analysed by ESI-MS and the chosen fractions were combined. Solvent was removed under reduced pressure.

pH determination. pH was determined by a HACH H138 minilab instrument. Three buffer solutions supplied: pH 4.01 ± 0.02 , 7.00 ± 0.02 and 10.01 ± 0.02 were used to calibrate the instrument. The probe was washed with deionised water between measuring samples. All the pH values were recorded at ambient temperature. The glass electrode was used without correction for the effect of deuterium. Meter readings for deuterated solvents (pH^*) were corrected to pH values using the equation: $\text{pH} = 0.929 \text{pH}^* + 0.41$.^{1, 5}

pH dependent studies of reactions of 1-I with GSH. Samples incubated at different pH were placed in 150 mM phosphate buffer (pH = 7.40) immediately before injection to the HPLC, in order to allow a uniform chromatographic analysis.

UV-visible spectroscopy. A Cary 300 UV-vis recording spectrophotometer was used with 1 cm path-length quartz cuvettes (0.5 mL) and a PTP1 Peltier temperature controller. Experiments were carried out at 288 K between 800-200 nm at a scan rate of 600 nm/min with 1 nm intervals unless otherwise stated. Spectra were recorded using UVWinlab software and processed using Origin 9.0.

Inductively coupled plasma optical emission spectroscopy (ICP-OES). ICP-OES analysis of osmium solutions were carried out on a Perkin Elmer (Optical Emission Spectrometer) Optima 5300 DV instrument. All samples and standards were prepared fresh on the day in doubly deionised water with distilled HNO_3 (3.2%).

The osmium standard was diluted to the following concentrations for the calibration curve: 0, 25, 50, 100, 200, 400, 600, 800 and 1000 ppb. The samples were diluted by serial dilutions of typically 1 in 10 until their concentrations fitted within the calibration range and the % total dissolved solids were below 0.2%. Samples were made in triplicate and the optical emission at 228.226 and 225.585 nm were detected and integrated. Data were acquired and processed using WinLab32 V3.4.1.

High performance liquid chromatography (HPLC). The HPLC analysis of complexes was carried out on an Agilent Technologies 1200 series HPLC instrument with a VWD detector module, and an injector unit connected to a 100 μ L loop. The instrument had attached an Agilent ZORBAX Eclipse Plus C18 250 x 4.6 mm column with a pore size of 5 μ m. Mobile phases consisted of: (A) H₂O with 0.1 % TFA, and (B) MeCN with 0.1 % TFA (HPLC grade materials were used). The solvent gradient described below was used, with a 1 mL/min flow rate. All the samples were prepared as aqueous solution and filtered through Iso-DisCTM filters (PTFE-4-4 4 mm x 0.45 μ m). Osmium imino complexes (**1-imp_y-I**) samples (ca. 50-100 μ M, 50 μ L) were injected into the HPLC instrument and analysed at a detection wavelength of 254 nm with reference wavelengths set to 360 nm and 510 nm. Osmium azo complexes (**1-CI** and **1-I**) samples (ca. 50-100 μ M, 50 μ L) were injected and analysed with a detection wavelength of 610 nm with a reference wavelength setting of 360 nm. The chromatograms were analysed using ChemStation software and any peaks greater than 10 mAU were integrated. Chromatograms were processed using Origin 9.0.

Time (min)	% (B) for azo complexes	% (B) for imino complexes
0	10	20
30	80	60
40	80	60
41	10	20
55	10	20

Liquid chromatography-mass spectrometry (LC-MS). A Bruker Amazon X+ instrument coupled with an Agilent Technologies 1200 series HPLC instrument and a VWD detector module was used. The same HPLC column, method and conditions were used as shown in HPLC part. Sample injections were 20 μ L with about 50-100 μ M concentrations and the mass spectrometer was operated in electrospray positive mode with a scan range of 50-2000 m/z. Data were processed using Bruker Compass DataAnalysis 4.4.

Nuclear magnetic resonance (NMR). ^1H NMR spectra were acquired at 400 MHz in 5 mm NMR tubes at 298 K on AV-400 spectrometer. Data processing was carried out using TOPSPIN version 2.1 (Bruker U.K. Ltd). ^1H NMR chemical shifts were internally referenced to TMS *via* their residual solvent peaks: methanol (δ = 3.31 ppm), water (δ = 4.79 ppm), DMSO (δ = 2.50 ppm). 1D ^1H NMR spectra were recorded using standard pulse sequences and acquired with 16 transients into 32 k data points over a spectral width of 14 ppm.

Elemental analysis. All purified complexes and ligands were analysed by elemental analysis. Analyses (carbon, hydrogen and nitrogen) were performed by Warwick Analytical Service using an Exeter Analytical elemental analyser (CE440).

High resolution mass spectrometry (HRMS). HR-MS analysis was carried with Bruker MaXis plus Q-TOF mass spectrometer equipped with an electrospray ionisation source. Mass spectrometer was operated in electrospray positive ion mode with a scan range 50-2,400 m/z. Source conditions: end plate offset at -500 V; capillary at -4000 V; nebulizer gas (N_2) at 0.5 bar; dry gas (N_2) at 4 L/min; dry Temperature at 453 K. Ion transfer conditions as: ion funnel RF at 200 Vpp; multiple RF at 200 Vpp; quadrupole low mass set at 50 m/z; collision energy at 5.0 eV for MS and 10-20 eV for MS/MS, MS/MS isolation window 10; collision RF at 500-2000 Vpp; transfer time set at 50-150 μ s; pre-Pulse storage time set at 5 μ s. Calibration was done with sodium formate (10 mM) before analysis. The HRMS spectra of complexes **1-Cl**, **1-I**, **1-NO₃**, **1-OH**, **1-SG**, **1-NAC**, **1-imp₁-Cl**, **1-imp₁-I** were obtained

from analysing isolated complexes solution (50 μM in 5 mM ammonium acetate buffer pH = 7.32). The HRMS spectra of **1-SOG** were obtained from analysing the reaction solution of **1-I** (50 μM) with GSH (1.25 mM) solution (in 5 mM ammonium acetate buffer pH = 7.32). The HRMS of **1-impy-OH** and **1-impy-SG** was obtained from **1-impy-Cl** (50 μM) with GSH (50 μM) solution (in 5 mM ammonium acetate buffer pH = 7.32).

pK_a determination for 1-OH. A 2 mM solution of **1-OH** was prepared in D₂O, and 4 mM dioxane was added as NMR standard reference (chemical shift is 3.75 ppm).⁶ The solution was aliquoted into 8 samples of 600 μL and the pH* values were adjusted sequentially by adding 1-10 μL of either KOD or DNO₃ (0.01, 0.1, 1, 2, 3, 4, 6, 8 or 10 M) in D₂O. pH values were measured over a range of 1.5 - 13.5 using a pH meter with correction for the effect of deuterium on the glass electrode. Changes in the chemical shifts of protons in complex **1-OH** were followed by ¹H NMR. The data were fitted to the Henderson-Hasselbalch equation using Origin 8.5, giving a pK_a value for **1-OH₂** of 5.20 ± 0.02 (Fig. S15).

XAS experimental setup and data collection strategies. X-ray absorption (XAS) experiments at the Os L₃-edge (10871 eV) were performed on the BM23 beamline of the European Synchrotron Radiation Facility (ESRF, Grenoble, France).⁷ XAS experiments were conducted in transmission mode, using a Si(111) double crystal monochromator to select the incident X-ray energy. The intensity of the incident beam I_0 and the beam transmitted through the sample (I_1) and a reference Hf metal foil (I_2) was monitored by 30 cm ionization chambers. Such a setup allowed a precise energy calibration for each collected XAS spectrum.

For static and *in situ* experiments in solution, a 4-mm thick EXAFS cell, specifically devoted to liquid samples, was filled with 30 mM solutions of **1-I** in pH 7 (200 mM phosphate buffer), pH 5 (200 mM citrate-phosphate buffer), or pH 3 (200 mM citrate-phosphate buffer) buffers, resulting in edge-jumps $\Delta\mu\text{x} \sim 0.3$ for a total absorption after the edge $\mu\text{x} \sim 2.2$. Initiation of the reaction for *in situ* experiments was obtained

by injecting GSH in the cell at Os : GSH molar ratios of 1:2 or 2:1, depending on the specific experiment. The solid-state structures of **1-I**, as well as those of the **1-SG**, **1-CI**, **1-OH** and OsCl₃ model compounds, were also characterized with transmission-mode XAS measurements, performed on self-supporting pellets of optimized mass. For studies on solid-state model compounds, we employed higher-quality scans in the 10639 – 12107 eV range, requiring ca. 40 min of data collection per spectrum. The pre-edge region and XANES part of the spectra were acquired with a constant energy step of 5 and 0.5 eV, respectively, while the EXAFS part (up to 18 Å⁻¹) was collected with a $\Delta k = 0.035 \text{ \AA}^{-1}$, resulting in a variable sampling step in energy. The integration time was 1 s/point for the pre-edge region and XANES regions, and quadratically variable from 1 to 8 s/point in the EXAFS part of the spectrum. For *in situ* experiments during **1-I** hydrolysis reaction, we adopted shorter scans (20 min per spectrum) in the 10724 – 11619 eV range. In this case, the integration time in the EXAFS region quadratically increased from 1 to 4 s/point, up to 14 Å⁻¹, while the energy sampling parameters in the pre-edge and XANES region were the same as for the longer scans. Notably, the first accessible time point after GSH injection corresponded to 40 min, including ca. 20 min to safely set the measurement and 20 min to collect of the first scan.

Energy calibration and alignment, normalization to the edge jump, and extraction of the $\chi(k)$ functions for all the collected spectra was performed using the Athena program.⁸ For static experiments, two or three consecutive EXAFS spectra were collected for each sample, and the corresponding $\mu x(E)$ curves were averaged, after checking the data reproducibility.

EXAFS fitting model and simulation strategy. The high-quality EXAFS spectra collected for **1-I** and **1-SG** in the solid state, as well as for pH 7, 5, and 3 buffer solutions of **1-I**, were fitted starting from the available DFT models. EXAFS fits were performed using the Artemis software.⁸ The fits were performed in R-space in the $\Delta R = 1.2\text{--}5.0 \text{ \AA}$ range, Fourier transforming the $k_2\chi(k)$ curves in the 2.0–15.5 Å⁻¹

range, resulting in 42 independent points. Phase and amplitude functions of each path were calculated using as starting guess the geometry of **1-I** or **1-SG** from computational analysis. To limit the number of optimized variables, the single scattering (SS) and multiple-scattering (MS) paths included in the fitting model were optimized with the same amplitude factor (S_{02}) and with the same energy shift (ΔE) parameter.

For both the Os-complexes, the fitting model included SS contributions from N_1 and C_1 sub-shells, involving two N atoms from the pyridylazolate unit and 6 C atoms from the *p*-cymene unit, respectively. The SS contributions from the iodido ligand in **1-I** and for the S ligand in **1-SG** were also included. For each of these coordination shells, the corresponding SS paths have been parametrized employing the same Debye-Waller (DW) factors σ_{2i} and bond distances R_i from Os absorber, with coordination number fixed to the DFT geometry.

A lower-level parametrization strategy was employed for the SS involving the farer C atoms of the pyridylazolate unit and the numerous MS paths falling in the 3.0–5.0 Å range from the Os center. These paths were parametrized by considering a common contraction/expansion factor α_{far} and a DW factor σ_{2far} increasing as the square root of the path length R_{eff} . This approach, allowing a significant reduction of the number of free fit parameters, has already been successfully used in the EXAFS analysis of metal complexes in solution as well as hosted in microporous matrixes, for which an initial structural model was available either from XRD or from computational modelling.^{9, 10} Details of the fitting results on solid-state compounds and buffer solutions of **1-I** are in Tables S7-S8 respectively.

The values of the optimized parameters obtained in these fits were employed to guide the simulation of the EXAFS signature for the **1-GS/NN** intermediate predicted by DFT (local environment in Fig. S31e). For the simulation, we calculated all the SS and MS paths resulting from the DFT geometry in the relevant R-space range 1.2–5.0 Å. Then, we parametrized the paths as described before for the fits, and fixed the eight relevant parameters (S_{02} , ΔE , ΔR_{N1} , σ_{2N1} , ΔR_{C1} , σ_{2C1} , α_{far} , σ_{2far}) based on the

best-fit values obtained for **1-I** and **1-SG**, as detailed in the last column of Table S7. The simulation was hence obtained by summing all the parametrized paths. The resulting EXAFS spectra in R-space and k-space are reported in Fig. S31f-g.

k-space Linear Combination Fit (LCF) analysis of in situ EXAFS. Linear combination fit (LCF) analysis of the k^2 -weighted time-dependent *in situ* EXAFS spectra was performed in k-space the 3.0–12.0 Å⁻¹ interval, using the Athena software from the Demeter package⁸ Each experimental scan, $k^2\chi_{\text{EXP}}(k)$, was fitted as a linear combination of reference EXAFS spectra, $k^2\chi_{\text{iREF}}(k)$, i.e.: $k^2\chi_{\text{iLCF}}(k) = \sum_i w_i k^2\chi_{\text{iREF}}(k)$, optimizing the weights w_i for each reference spectrum. LCF was performed by setting the total sum of the weights to unity, $\sum_i w_i = 1$ and constraining the weights in the [0 ; 1] interval ($0 \leq w_i \leq 1$). For each analysed scan, the corresponding LCF R-factor was computed as $\sum_j [k^2\chi_{\text{EXPj}} - k^2\chi_{\text{LCFj}}]^2 / \sum_j [k^2\chi_{\text{EXPj}}]^2$, where j denotes each experimental point in fitted k-range, 3.0–12.0 Å⁻¹; R-factor = 0 corresponds to the ideal reproduction of the experimental curve: $k^2\chi_{\text{EXP}}(k) \equiv k^2\chi_{\text{LCF}}(k)$. Reference spectra were selected for each specific *in situ* experiment based on the examination of the EXAFS features of the experimental data series.

Computational details. The Gaussian 09 program¹¹ was employed to carry out all calculations in the framework of density functional theory using the hybrid Becke three-parameter exchange functional¹² and the Lee–Yang–Parr correlation functional, B3LYP.¹³ Dispersion corrections for nonbonding interactions were included through the Grimme approach using atom pair-wise additive schemes, DFT-D3 method.¹⁴

LANL2DZ effective core potential was used for the Os atom,¹⁵ along with the split valence basis set. The standard triple- ζ quality 6-311+G** basis sets of Pople and coworkers were used for the atoms directly participating in the process, whereas in order to reduce the computational effort, the 6-31G* basis sets were employed for peripheral atoms. Vibrational frequencies at the same level of theory were calculated for both establishing the nature of intercepted stationary points as minima and transition states and calculating zero-point energy (ZPE) and Gibbs free energy

corrections. The intercepted transition states are first order saddle points on a potential energy surface (PES) and their vibrational spectrum is characterized by one imaginary frequency, corresponding to a negative force constant, which means that in one direction, in the nuclear configuration space, the energy has a maximum, while in all the other directions the energy has a minimum. Furthermore, transition states were carefully checked to be properly connected to the correct minima by IRC (intrinsic reaction coordinate) analysis.^{16, 17}

The Tomasi's implicit Polarizable Continuum Model (PCM)^{18, 19} as implemented in Gaussian09 has been used to include the effects due to the presence of the solvent and the UFF set of radii has been used to build-up the cavity in which the solute molecules are accommodated. Solvation Gibbs free energies were calculated performing single-point calculations for all *in vacuo* stationary points structures in implicit water ($\epsilon=78.4$) at the same level of theory. Enthalpies and Gibbs free energies were obtained using standard statistical procedures²⁰ at 298 K and 1 atm from total energies, including zero-point, thermal and solvent corrections. As the free energy corrections in the Gaussian's default standard state corresponds to an ideal gas at a standard pressure of 1 atm, the computed free energies were converted to yield Gibbs energies with a solution phase standard state of 1 mol L⁻¹ for all the species except water solvent.²¹ For water molecules a standard state of 55.5 M was used. That is, to the free energy of each species, as computed in Gaussian, a free energy correction term equal to $RT \ln(V_{\text{molar gas}}/V_{\text{molar solution}})$, (R = gas constant, T = absolute temperature) has been added, where $V_{\text{molar gas}}$ is the volume occupied by one mole of ideal gas at the considered temperature, and $V_{\text{molar solution}}$ is the volume occupied by one mole of species in a standard solution of concentration 1 mol L⁻¹.

Tables

Table S1. Species identified by HPLC/LC-MS/HRMS and their molecular formulae, calculated and observed m/z values, and HPLC retention times (the solvent gradient used can be found in page S11).

Species	Molecular formula	Calculated m/z	Observed m/z (LCMS)	Observed m/z (HRMS)	HPLC retention time (min)
[1-I] ⁺	C ₂₃ H ₂₈ IN ₄ Os ⁺	679.0969	679.02	679.0952	23.02
[1-Cl] ⁺	C ₂₃ H ₂₈ ClN ₄ Os ⁺	587.1602	587.21	587.1594	19.67
[1-imp _y -Cl] ⁺	C ₂₄ H ₂₉ ClN ₃ Os ⁺	586.1649	586.23	586.1633	26.43*
[1-imp _y -I] ⁺	C ₂₄ H ₂₉ IN ₃ Os ⁺	678.1016	678.17	678.1028	41.42*
[1-NO ₃] ⁺	C ₂₃ H ₂₈ N ₅ O ₃ Os ⁺	614.1802	614.11	614.1809	18.62
[1-NAC + H] ⁺	C ₂₈ H ₃₆ N ₅ O ₃ SOs ⁺	714.2147	714.16	714.2149	15.68
[1-OH] ⁺	C ₂₃ H ₂₉ N ₄ OOs ⁺	569.1951	569.17	569.1941	12.53
[1-imp _y -OH] ⁺	C ₂₄ H ₃₀ N ₃ OOs ⁺	568.1999	568.23	568.1999	11.30*
[1-SG + H] ⁺	C ₃₃ H ₄₄ N ₇ O ₆ OsS ⁺	858.2682	858.19	858.2693	13.29
[1-imp _y -SG + H] ⁺	C ₃₄ H ₄₅ N ₆ O ₆ OsS ⁺	857.2730	857.11	857.2738	12.44*
[1-SOG + H] ⁺	C ₃₃ H ₄₄ N ₇ O ₇ OsS ⁺	874.2632	874.15	874.2634	11.54

* The HPLC methods for imino complexes and azo complexes are different (see page S11).

Table S2. Extinction coefficients for osmium complexes at 610 nm

Complex	E ₆₁₀ (M ⁻¹ cm ⁻¹)
1-Cl	25000±122
1-I	41000±217
1-NAC	21000±141
1-SG	26000±435
1-OH	28000±237

Table S3. Percentage (%) of osmium species (**1-I**, **1-Cl**, **1-OH**, **1-SG** and **1-SOG**) observed using HPLC (the solvent gradient used can be found in page S11) in the reaction of **1-I** (75 μ M) with GSH (1.88 mM; 25 mol equiv) after 5 min, 1 h, 3 h, 6 h, 18 h, 24 h in 25 mM NaCl, 75 mM phosphate buffer solution (pH=7.40), corresponding to Fig. S19.

Time	Percentage of Osmium Species (%) ^a				
	1-I	1-Cl	1-OH	1-SG	1-SOG
5 min	100.00 \pm 3.50	0	0	0	0
1 h	83.09 \pm 2.91	0.88 \pm 0.03	16.03 \pm 0.59	0	0
3 h	50.45 \pm 1.77	3.58 \pm 0.11	30.38 \pm 1.12	15.59 \pm 0.70	0
6 h	26.22 \pm 0.92	4.08 \pm 0.13	33.63 \pm 1.24	36.07 \pm 1.62	0
18 h	5.62 \pm 0.20	1.69 \pm 0.05	18.47 \pm 0.68	70.47 \pm 3.17	3.75 \pm 0.17
24 h	4.23 \pm 0.19	1.35 \pm 0.04	16.54 \pm 0.61	68.23 \pm 3.07	9.65 \pm 0.43

^a mean \pm sd

Table S4. Percentage (%) of osmium species (**1-Cl**, **1-OH**, **1-SG** and **1-SOG**) observed using HPLC (the solvent gradient used can be found in page S11) in the reaction of **1-Cl** (75 μ M) with GSH (0.94 mM; 12.5 mol equiv) after 5 min, 1 h, 3 h, 6 h, 18 h, 24 h in 25 mM NaCl, 75 mM phosphate buffer solution (pH=7.40) (Corresponding with Fig. S20).

Time	Percentage of Osmium Species (%) ^a			
	1-Cl	1-OH	1-SG	1-SOG
5 min	97.17 \pm 3.05	2.83 \pm 0.11	0	0
1 h	16.21 \pm 0.51	83.79 \pm 3.10	0	0
3 h	8.70 \pm 0.27	77.09 \pm 2.85	14.21 \pm 0.64	0
6 h	6.34 \pm 0.20	68.10 \pm 2.52	25.56 \pm 1.15	0
18 h	2.87 \pm 0.09	41.01 \pm 1.52	36.92 \pm 1.66	19.20 \pm 0.86
24 h	1.96 \pm 0.06	36.81 \pm 1.36	33.25 \pm 1.50	27.98 \pm 1.26

^a mean \pm sd

Table S5. Percentage (%) of osmium species (**1-I**, **1-CI**, **1-OH**, **1-SG** and **1-NAC**) observed using HPLC (the solvent gradient used can be found in page S11) after reactions of **1-I** (75 μ M) with thiols GSH, NAC or DTT (0.75 mM; 10 mol equiv) in 25 mM NaCl and 75 mM phosphate buffer (pH 7.4) at 310 K for 24 h (corresponding to Fig. S23 and S24).

Thiol	Percentage of Osmium Species (%) ^a				
	1-I	1-CI	1-OH	1-SG	1-NAC
Buffer	99.87 \pm 3.50	0	0.13 \pm 0.01	0	0
GSH	16.07 \pm 0.56	4.15 \pm 0.13	78.80 \pm 2.92	0.98 \pm 0.04	0
DTT	34.57 \pm 1.21	0	65.53 \pm 2.42	0	0
NAC	10.13 \pm 0.35	3.32 \pm 0.11	57.04 \pm 2.11	0	29.51 \pm 1.33

^a mean \pm sd

Table S6. Percentage (%) of osmium species (**1-I**, **1-OH** and **1-SG**) observed using HPLC (the solvent gradient used can be found in page S11) after incubation of **1-I** (100 μ M) with GSH (200 μ M; 2 mol equiv) for 3 h and 6 h at 310 K at various pH values (pH= 2.43, 6.86 and 10.05) (corresponding to Fig. S26).

Time	pH value	Percentage of Osmium Species (%) ^a		
		1-I	1-OH	1-SG
3 h	2.43	99.40 \pm 3.48	0.60 \pm 0.02	0
	6.86	86.22 \pm 3.02	13.78 \pm 0.51	0
	10.05	55.39 \pm 1.94	44.61 \pm 1.65	0
6 h	2.43	99.26 \pm 3.47	0.74 \pm 0.03	0
	6.86	72.83 \pm 2.55	23.87 \pm 0.88	3.30 \pm 0.15
	10.05	24.24 \pm 0.85	72.85 \pm 2.70	2.91 \pm 0.13

^a mean \pm sd

Table S7. Optimised parameters from EXAFS fitting of **1-I** and **1-SG** in the solid state, employed as initial data for the respective DFT geometries. The fit was performed in R-space in the range (1.2 – 5.0) Å, Fourier-transforming the $k_2\chi(k)$ functions in the (2.0 – 15.5) Å⁻¹ range. Selected DFT bond distances are also listed in bold, for comparison. The last column contains spectroscopic and structural parameters employed in the DFT-assisted simulation of the EXAFS spectrum for the **1-GS/NN** intermediate (structure in Fig. S31e). For each *i*th shell of scattering atoms, both the optimised (average) bond distances R_i and the corresponding radial shifts from DFT values [ΔR_i] are given. For details of the meaning of the other optimised parameters, see page S13.

Parameter	1-I		1-SG		1-GS/NN	
	DFT	Solid state ref.	DFT	Solid state ref.	DFT	Sim. parameters
S_{02}	–	0.72 ± 0.03	–	0.74 ± 0.4	–	0.75
ΔE (eV)	–	9 ± 1	–	9 ± 1	–	9
R-factor	–	0.00964	–	0.01588	–	–
n° <i>par./n</i> ^o <i>ind.</i>	–	10/32	–	10/32	–	–
<i>Corr. > 0.8</i>	–	σ_{2N} & $\sigma_{2C} \rightarrow$ 0.8175	–	None	–	–
$\langle R_{N1} \rangle$ [ΔR_{N1}] (Å)	2.056	2.06 ± 0.03 [+ 0.004]	2.061	2.03 ± 0.01 [+ 0.03]	1.983	2.000 [+ 0.017] ^(a)
σ_{2N1} (Å ²)	–	0.0011 ± 0.0008	–	$0.0025 \pm$ 0.0006	–	$0.003^{(d)}$
$\langle R_{C1} \rangle$ [ΔR_{C1}] (Å)	2.268	2.22 ± 0.01 [– 0.048]	2.297	2.22 ± 0.01 [– 0.077]	2.237	2.175 [– 0.062] ^(b)
σ_{2C1} (Å ²)	–	0.0015 ± 0.0008	–	0.004 ± 0.001	–	$0.004^{(d)}$
R_S [ΔR_S] (Å)	–	–	2.443	2.39 ± 0.01 [– 0.059]	–	–
σ_{2S} (Å ²)	–	–	–	$0.0022 \pm$ 0.0006	–	–
R_I [ΔR_I] (Å)	2.765	2.708 ± 0.004 [– 0.057]	–	–	–	–
σ_{2I} (Å ²)	–	0.0022 ± 0.0003	–	–	–	–
α_{far}	–	-0.009 ± 0.005	–	-0.022 ± 0.006	–	$-0.015^{(c)}$
σ_{2far} (Å ²)	–	0.005 ± 0.002	–	0.006 ± 0.003	–	$0.006^{(d)}$

(a) Obtained as the average of the ΔR_{N1} best-fit values for the **1-I** and **1-SG** solid-state references.

(b) Obtained as the average of the ΔR_{C1} best-fit values for the **1-I** and **1-SG** solid-state references.

(c) Obtained as the average of the α best-fit values for the **1-I** and **1-SG** solid-state references.

(d) Fixed for each sub-shell to the maximum best-fit value obtained in the fits of **1-I** and **1-SG** solid-state references.

Table S8. Best-fit parameters optimised in the EXAFS fit for the k_2 -weighted spectra of 30 mM buffer solutions of **1-I** at pH 7, pH 5 and pH 3, employed as starting structures in the fitting procedure for the DFT-optimized geometry. The fit was performed in R-space, in the range (1.2 – 5.0) Å, employing the k-range (2.0 – 15.5) Å⁻¹ for the FT. Selected bond distances from DFT are also given for comparison.

EXAFS fit parameter	1-I DFT	1-I (30 mM, pH 7)	1-I (30 mM, pH 5)	1-I (30 mM, pH 3)
S_{02}	–	0.75 ± 0.07	0.81 ± 0.05	0.79 ± 0.05
ΔE (eV)	–	9 ± 1	9 ± 1	8 ± 1
R-factor	–	0.02960	0.01594	0.02586
$N^\circ \text{ par.}/N^\circ \text{ ind.}$	–	10/32	10/32	10/32
Corr. > 0.8		σ_{2N} & $\sigma_{2C} \rightarrow 0.8124$	–	–
$\langle R_{N1} \rangle$ (Å)	2.056	2.06 ± 0.03	2.06 ± 0.03	2.02 ± 0.01
σ_{2N1} (Å ²)		0.003 ± 0.001	0.003 ± 0.001	0.002 ± 0.001
$\langle R_{C1} \rangle$ (Å)	2.268	2.21 ± 0.01	2.21 ± 0.01	2.21 ± 0.01
σ_{2C1} (Å ²)		0.003 ± 0.002	0.003 ± 0.001	0.002 ± 0.001
R_I (Å)	2.765	2.711 ± 0.007	2.704 ± 0.005	2.706 ± 0.008
σ_{2I} (Å ²)		0.0027 ± 0.0006	0.0026 ± 0.0004	0.0018 ± 0.0004
α		-0.01 ± 0.01	-0.010 ± 0.007	-0.02 ± 0.01
σ_2 (Å ²)		0.005 ± 0.004	0.006 ± 0.003	0.006 ± 0.004

Table S9. Os speciation during *in situ* XAS study of **1-I** hydrolysis at pH 7 and Os:GSH = 1:2 from LCF analysis of the EXAFS scans collected at representative time points. LCF performed on $k_2\chi(k)$ curves, in the range (3.0-12.0) Å⁻¹. Dominant contributions from **1-SG** and **1-CI** are highlighted in bold font.

LCF results	Concentration (% total Os)		
	40 min	80 min	220 min
1-I	9 ± 3	8 ± 3	7 ± 3
1-SG	63 ± 5	54 ± 4	50 ± 5
1-CI	22 ± 5	33 ± 4	42 ± 5
1-OH	6 ± 8	6 ± 7	2 ± 7
R-factor	0.0148	0.0093	0.0114

Table S10. Concentrations of **1-I**, **1-OH** and **GSH** at different time points (5-120 min) based on ¹H NMR peak integration (Fig. S40) for the reaction of **1-I** (2 mM) with **GSH** (200 μM, 10% mol equiv) in phosphate buffer (75 mM, pH 7.40) after various reaction times at 298 K under N₂.

Time (min)	Concentration (mM) ^a		
	1-I	1-OH	GSH
5	2.00±0.01	0	0.20±0.01
20	1.92±0.01	0.03±0.01	0.20±0.01
40	1.66±0.01	0.29±0.01	0.20±0.01
60	1.48±0.01	0.47±0.01	0.20±0.01
80	1.44±0.02	0.51±0.01	0.20±0.01
100	1.43±0.01	0.52±0.01	0.20±0.01
120	1.42±0.01	0.53±0.01	0.20±0.01

^a mean±sd

Figures

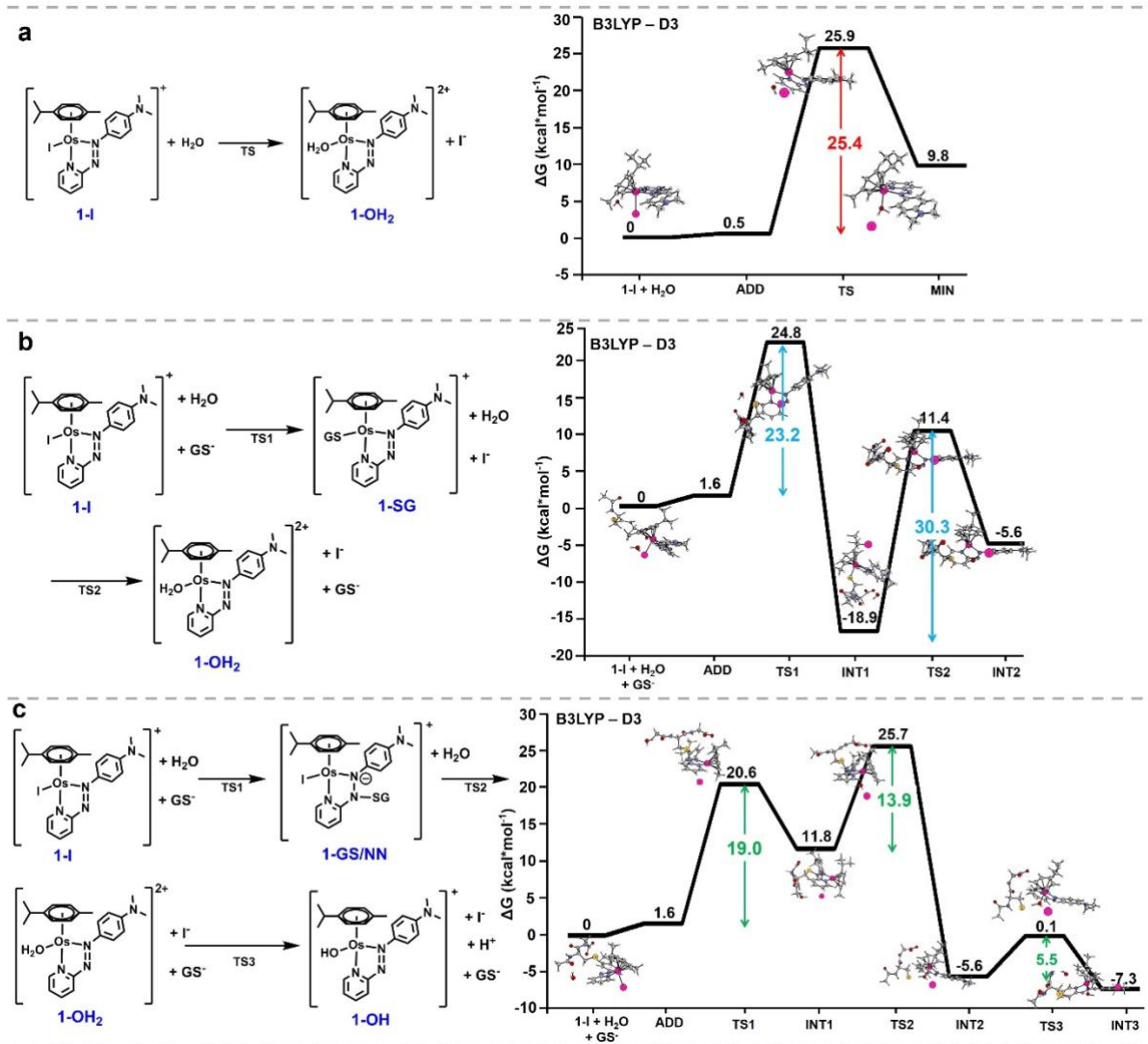
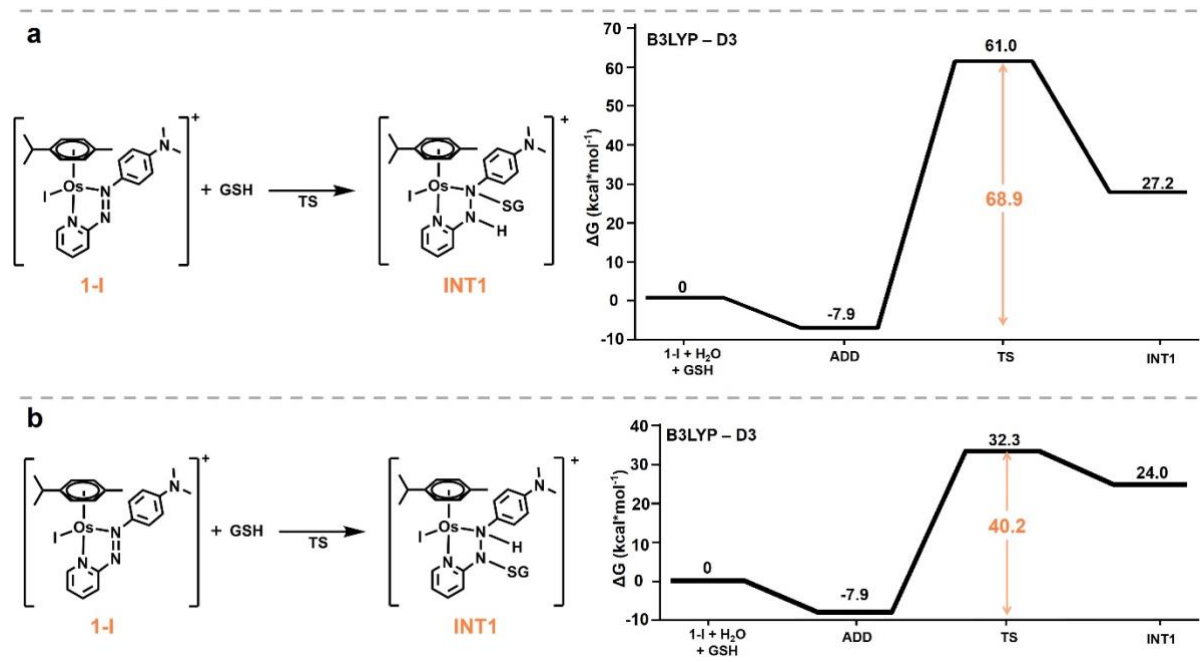


Fig.S1. DFT free energy profiles describing reaction pathways for **1-I** with GS^- . Relative energies are in kcal mol^{-1} and calculated with respect to the reference energy of separated reactants.



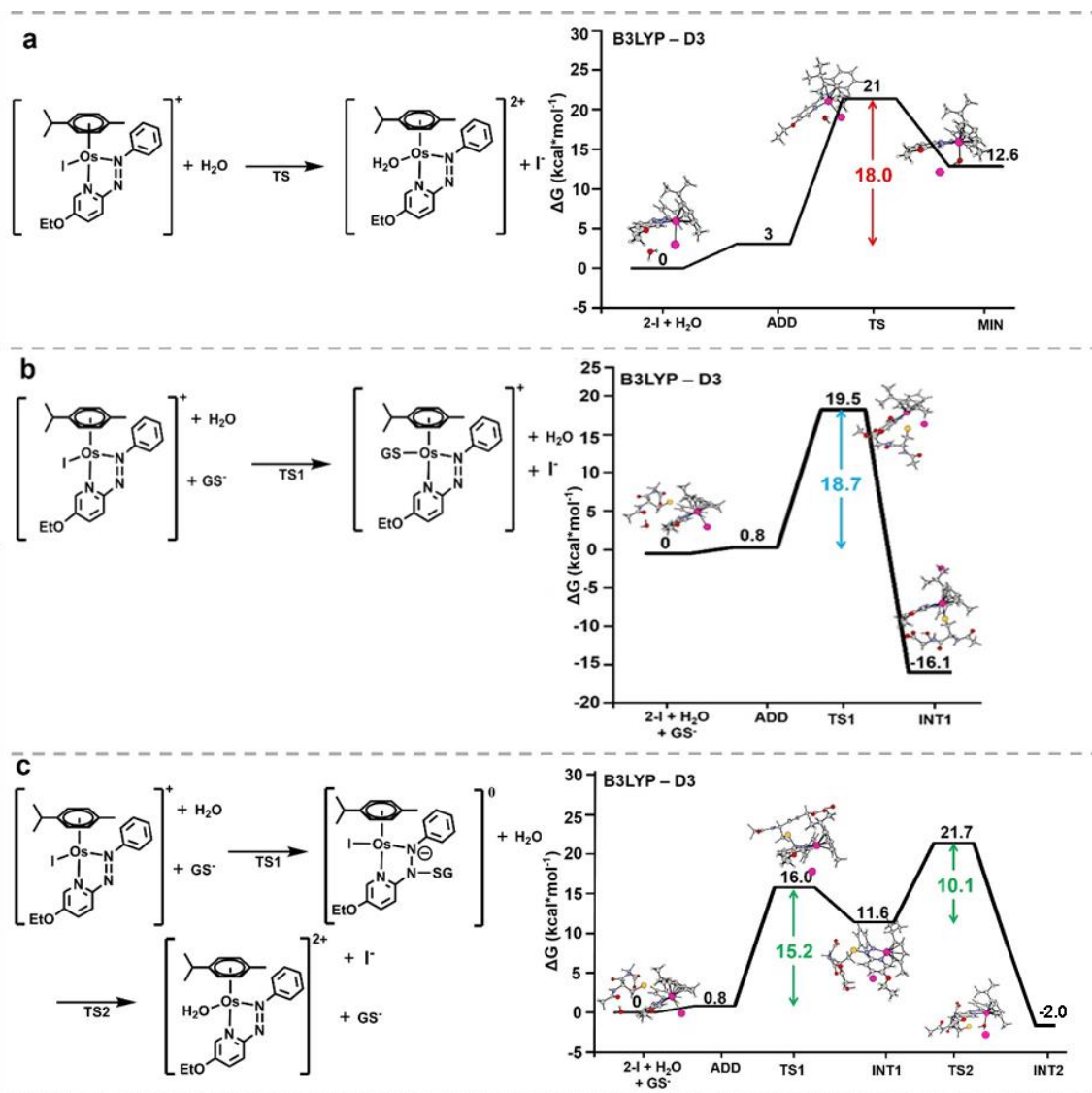


Fig. S3. DFT free energy profiles describing reaction pathways for **2-I** with GS^- . Relative energies are in kcal mol^{-1} and calculated with respect to the reference energy of separated reactants.

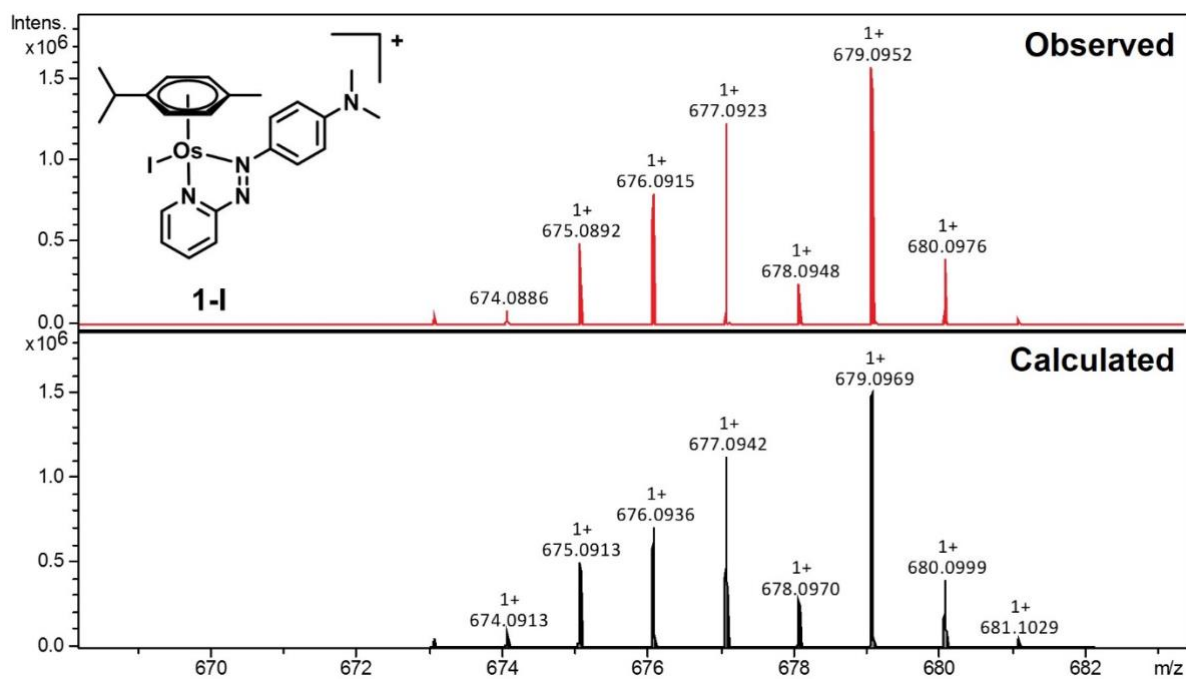


Fig. S4. HRMS spectra for **1-I**. Molecular formula: $C_{23}H_{28}IN_4Os^+$, calculated m/z: 679.0969, observed m/z: 679.0952, error: 2.5 ppm.

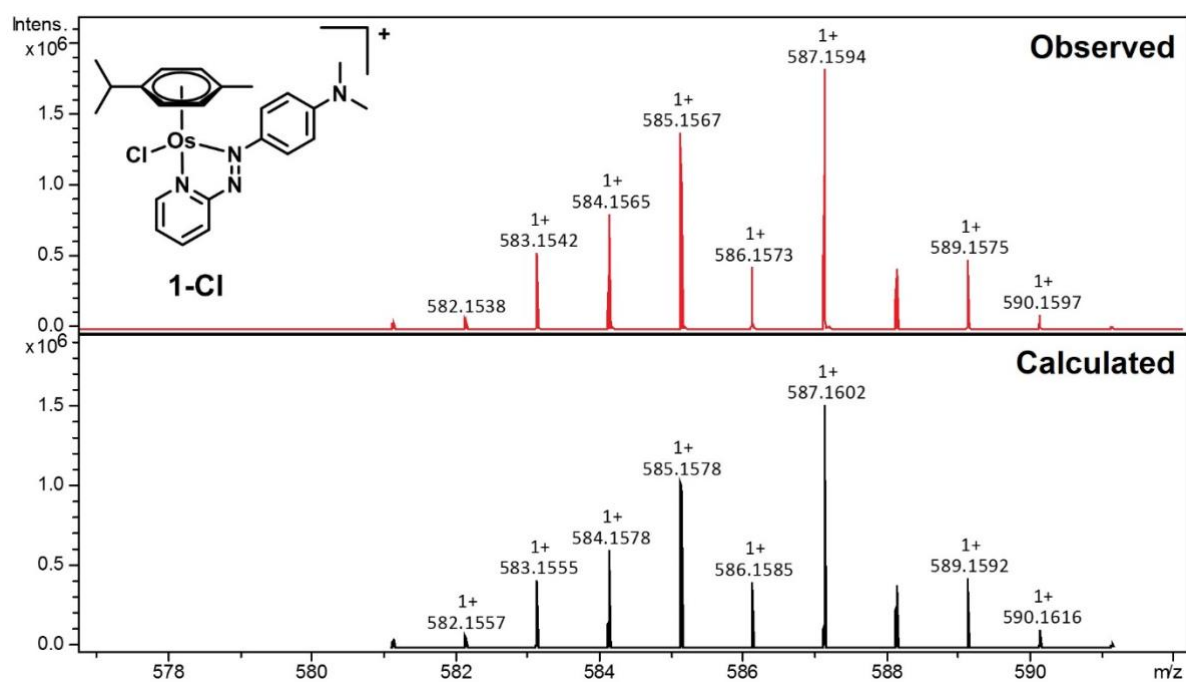


Fig. S5. HRMS spectra for **1-Cl**. Molecular formula: $C_{23}H_{28}ClN_4Os^+$, calculated m/z: 587.1602, observed m/z: 587.1594, error: 1.4 ppm.

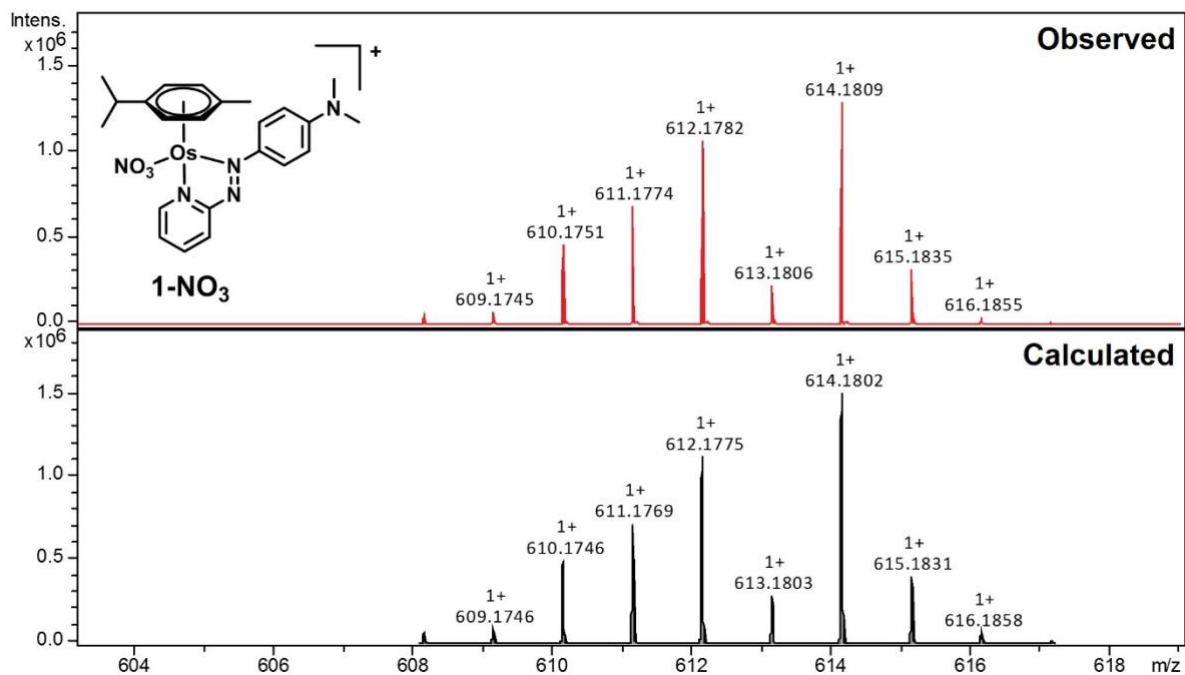


Fig. S6. HRMS spectra for **1-NO₃**. Molecular formula: C₂₃H₂₈N₅O₃Os⁺, calculated m/z: 614.1802, observed m/z: 614.1809, error: 1.2 ppm.

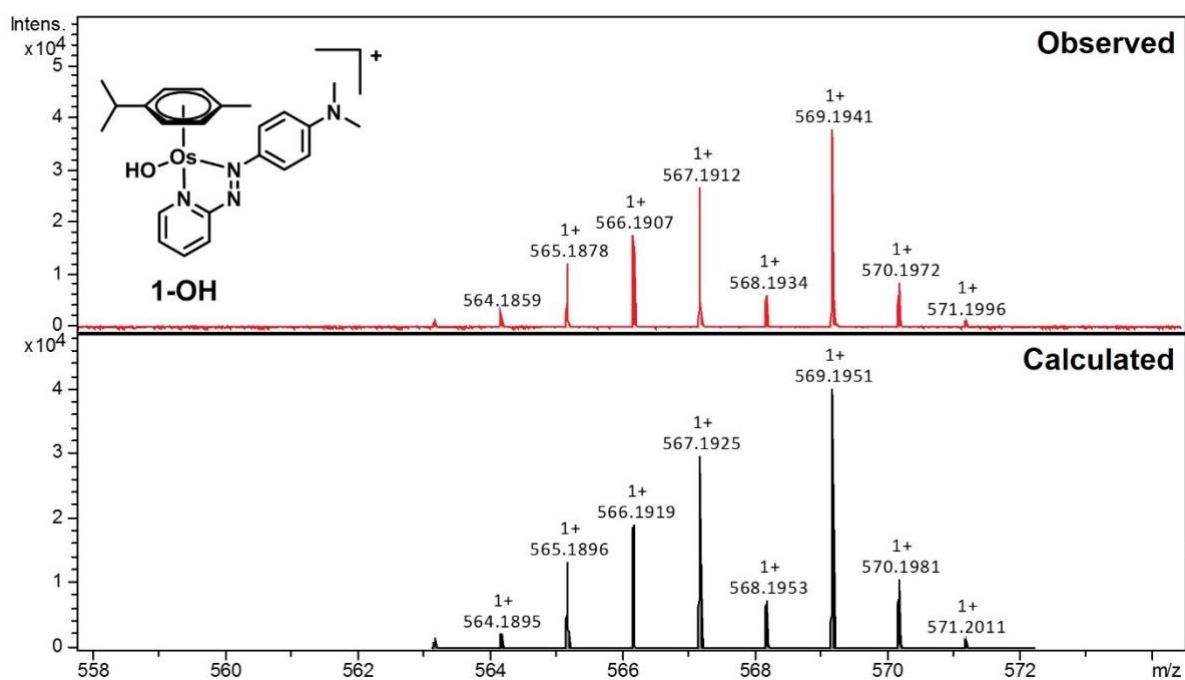


Fig. S7. HRMS spectra for **1-OH**. Molecular formula: C₂₃H₂₉N₄OOs⁺, calculated m/z: 569.1951, observed m/z: 569.1941, error: 1.8 ppm.

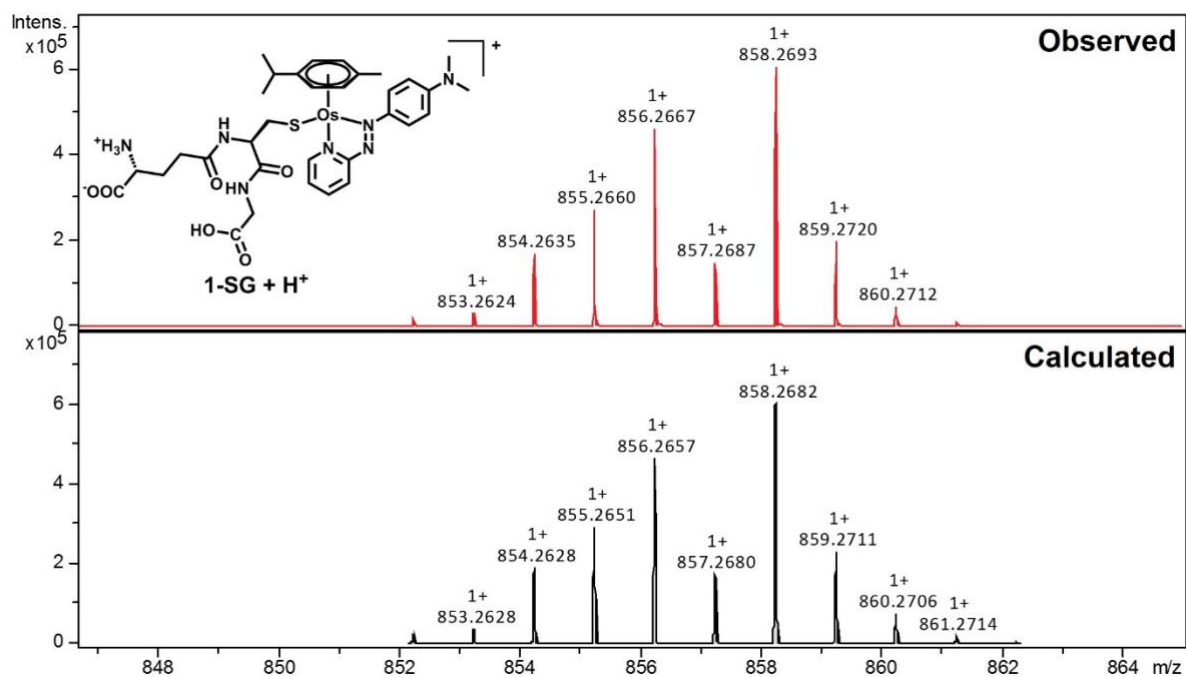


Fig. S8. HRMS spectra for **1-SG + H⁺**. Molecular formula: C₃₃H₄₄N₇O₆OsS⁺, calculated m/z: 858.2682, observed m/z: 858.2693, error: 1.3 ppm.

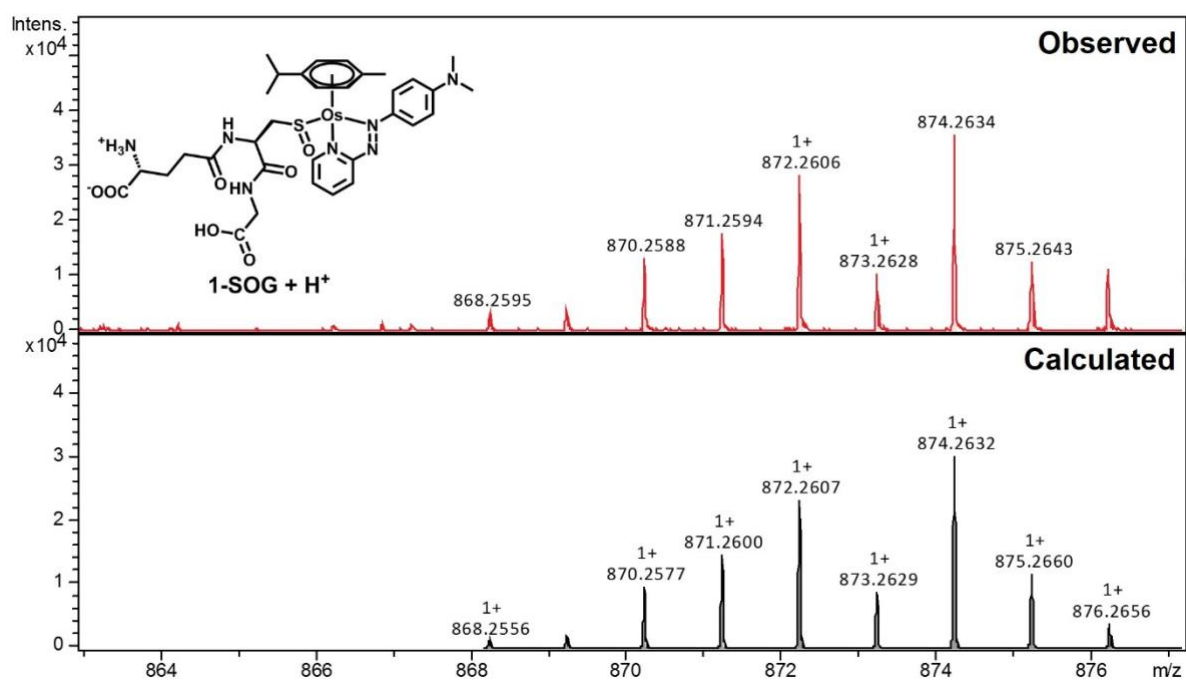


Fig. S9. HRMS spectra for **1-SOG + H⁺**. Molecular formula: C₃₃H₄₄N₇O₇OsS⁺, calculated m/z: 874.2632, observed m/z: 874.2634, error: 0.2 ppm.

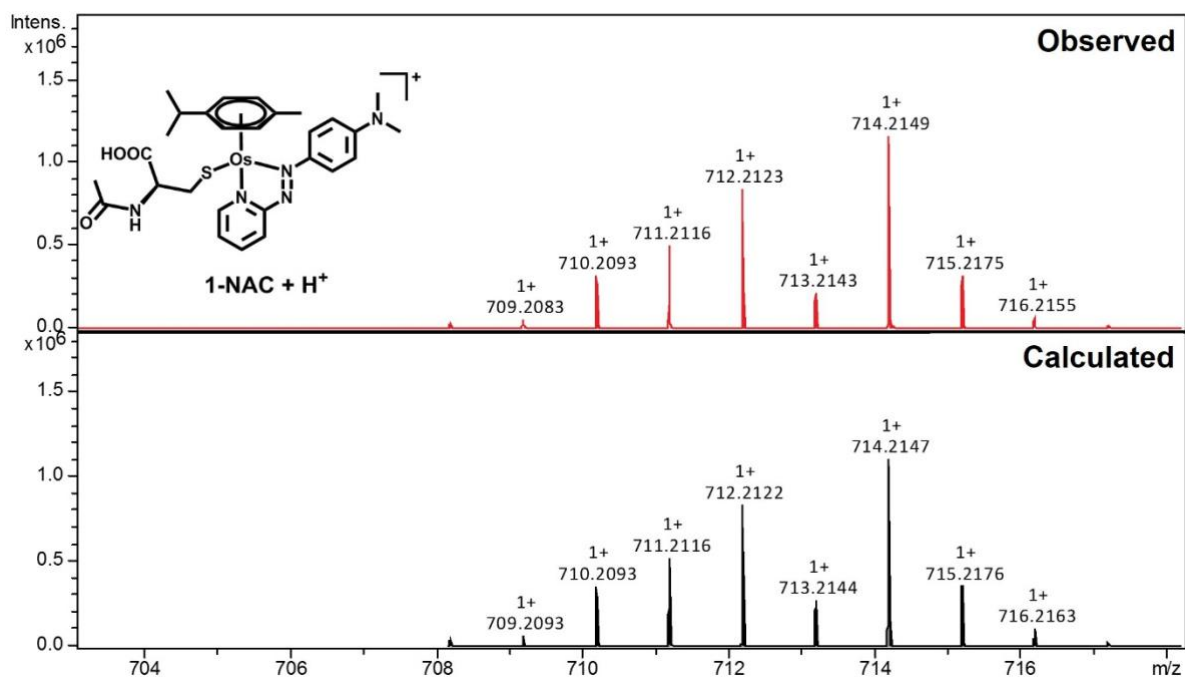


Fig. S10. HRMS spectra for **2-NAC + H⁺**. Molecular formula: C₂₈H₃₆N₅O₃OsS⁺, calculated m/z: 714.2147, observed m/z: 714.2149, error: 0.3 ppm.

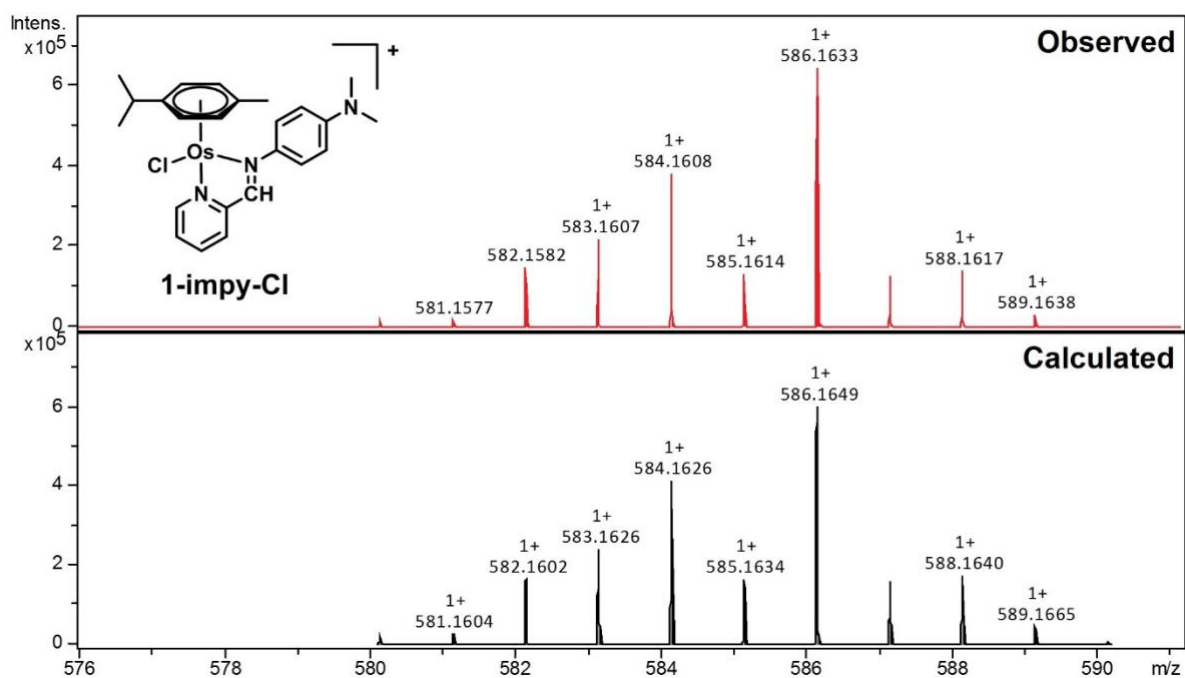


Fig. S11. HRMS spectra for **1-imp-y-Cl**. Molecular formula: C₂₄H₂₉ClN₃Os⁺, calculated m/z: 586.1649, observed m/z: 586.1633, error: 2.7 ppm.

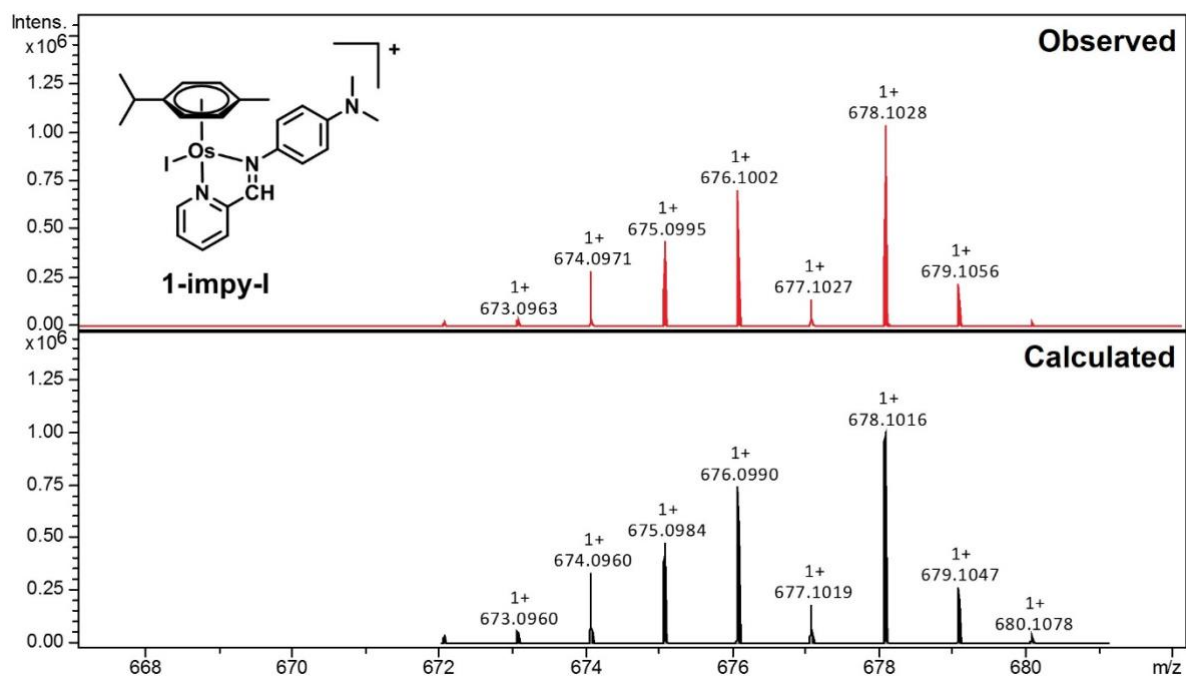


Fig. S12. HRMS spectra for **1-impy-I**. Molecular formula: $C_{24}H_{29}IN_3Os^+$, calculated m/z: 678.1016, observed m/z: 678.1028, error: 1.8 ppm.

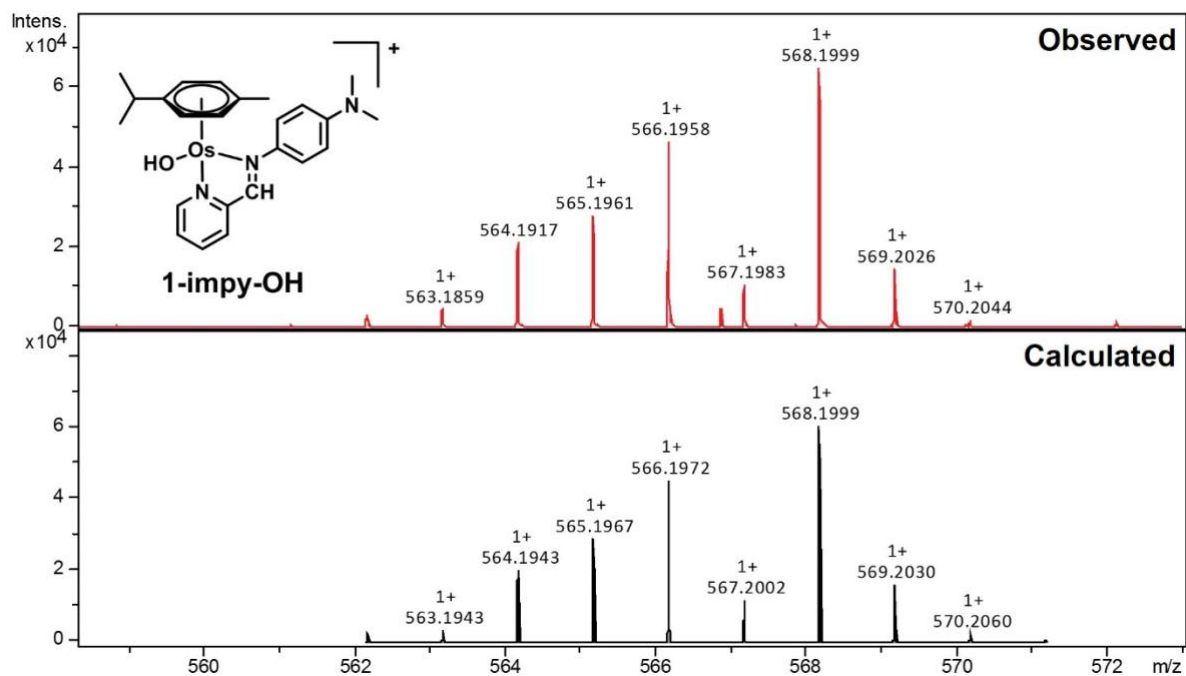


Fig. S13. HRMS spectra for **1-impy-OH**. Molecular formula: $C_{24}H_{30}N_3OOs^+$, calculated m/z: 568.1999, observed m/z: 568.1999, error: 0 ppm.

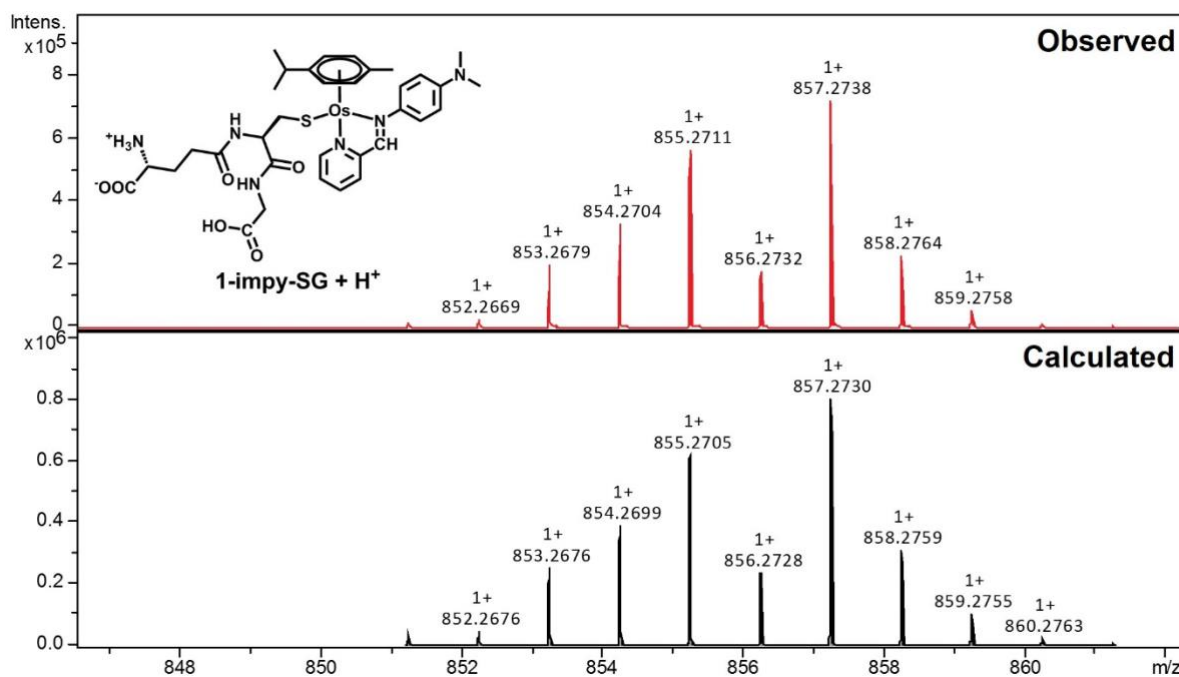


Fig. S14. HRMS spectra for **2-impY-SG + H⁺**. Molecular formula: C₃₄H₄₅N₆O₆OsS⁺, calculated m/z: 857.2730, observed m/z: 857.2738, error: 0.8 ppm.

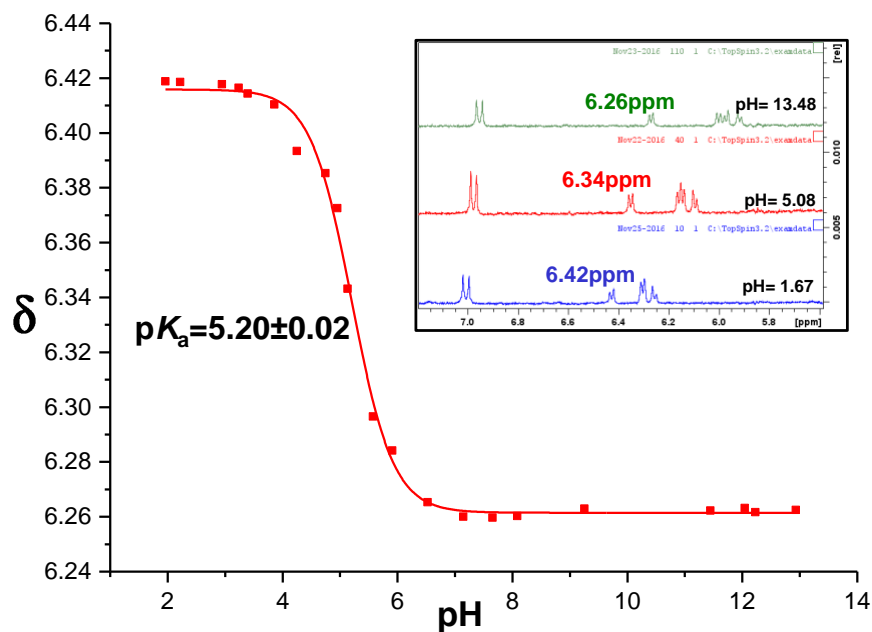


Fig. S15. Variation of the chemical shift of an aromatic *p*-cym proton of **1-OH** with pH. The red line represents a computer best fit to the Henderson-Hasselbalch equation.

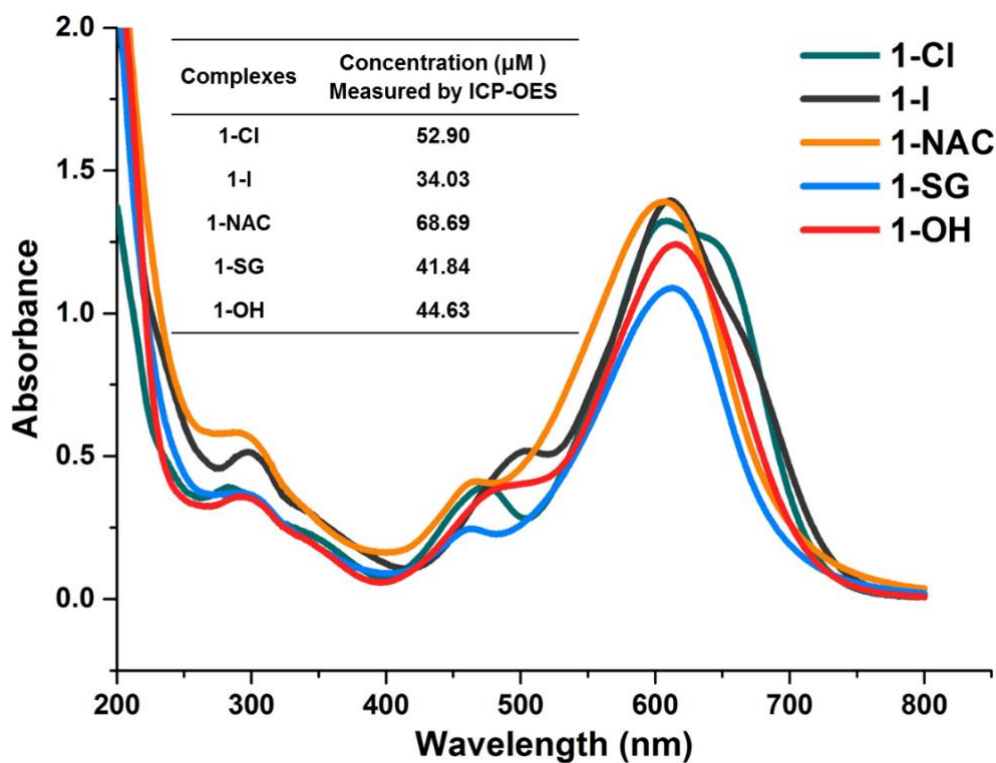


Fig. S16. UV-Vis spectra acquired from aqueous solutions of osmium complexes **1-Cl** (52.90 μM), **1-I** (34.03 μM), **1-NAC** (68.69 μM), **1-SG** (41.84 μM), **1-OH** (44.63 μM).

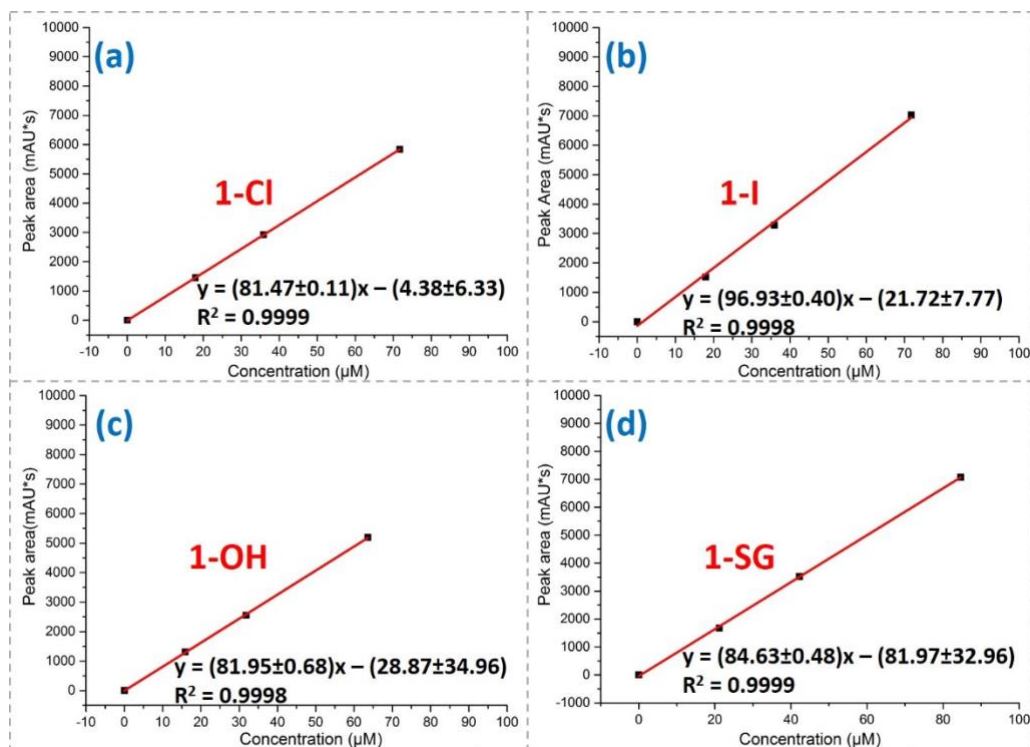


Fig. S17. Linear relationship of HPLC peak area (610 nm) and concentrations of **1-Cl** (a), **1-I** (b), **1-OH** (c) and **1-SG** (d).

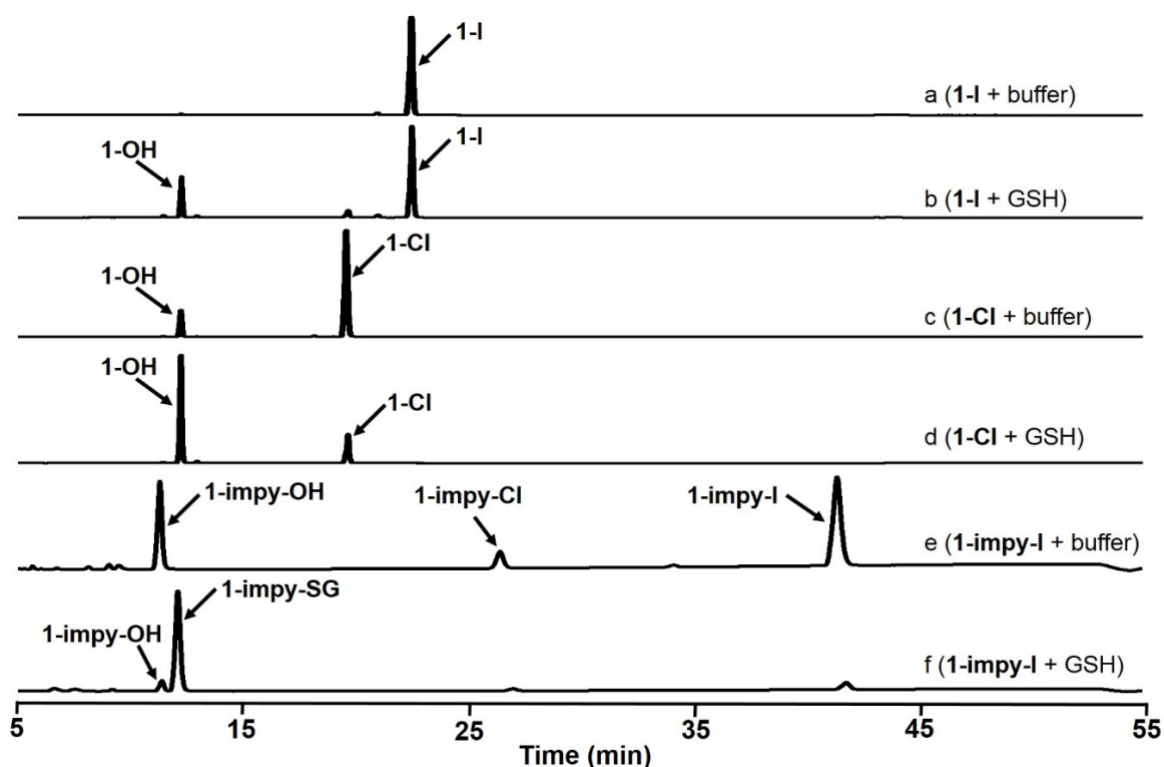


Fig.S18. HPLC traces showing products formed by the reaction of **1-I**, **1-Cl** or **1-imp-y-I** (75 μ M) with GSH (75 μ M; 1 mol equiv) in 25 mM NaCl and 75 mM phosphate buffer (pH 7.4) at 310 K for 24h. The solvent gradient used can be found in page S11.

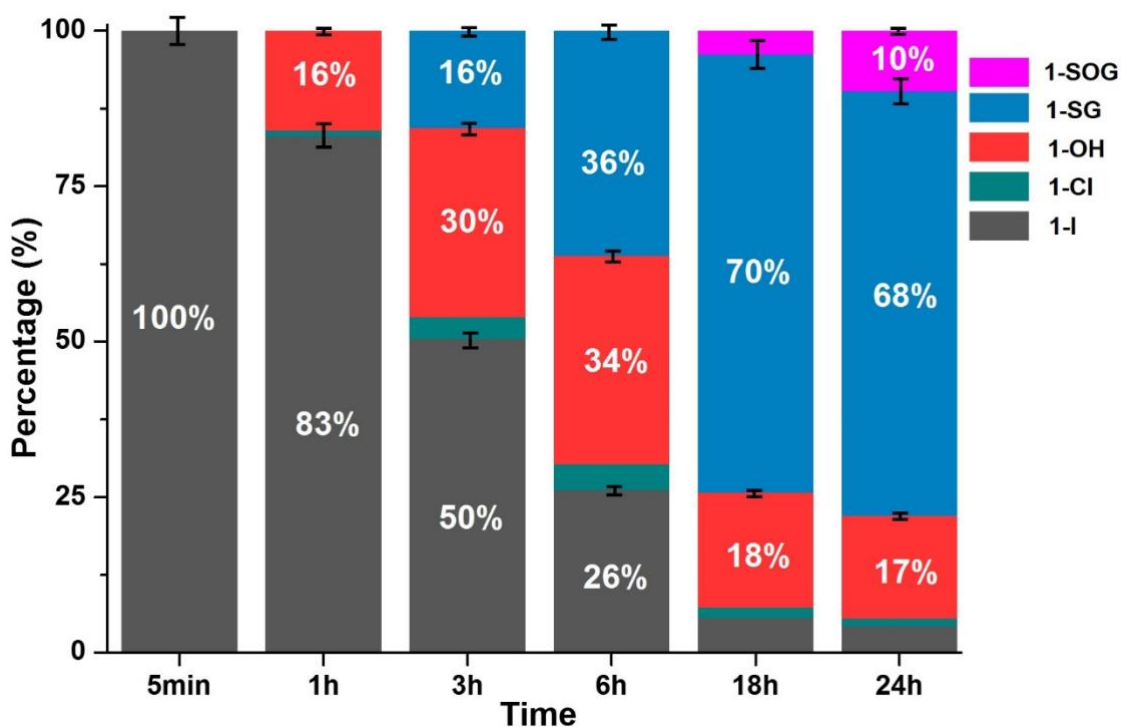


Fig. S19. Percentage of osmium species observed using HPLC (the solvent gradient used can be found in page S11) in the reaction of **1-I** (75 μ M) with GSH (1.88 mM; 25 mol equiv) after 5 min, 1 h, 3 h, 6 h, 18 h, 24 h in 25 mM NaCl, 75 mM phosphate buffer solution (pH=7.40).

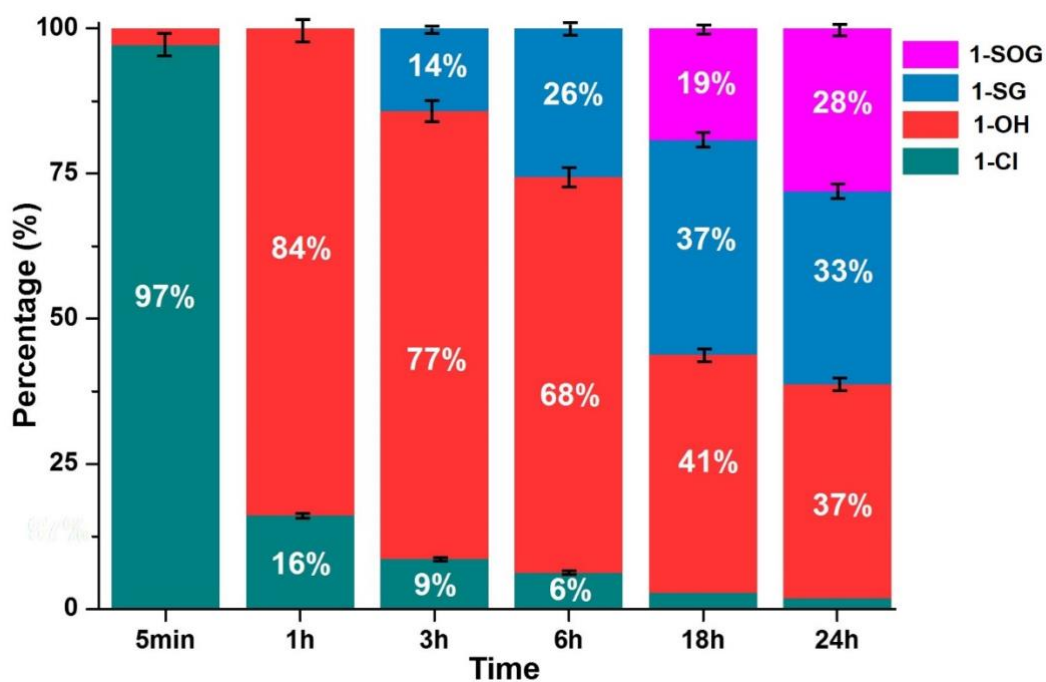


Fig. S20. Percentage of osmium species observed using HPLC (the solvent gradient used can be found in page S11) in the reaction of **1-Cl** (75 μ M) with GSH (0.94 mM; 12.5 mol equiv) after 5 min, 1 h, 3 h, 6 h, 18 h, 24 h in 25 mM NaCl, 75 mM phosphate buffer solution (pH = 7.40).

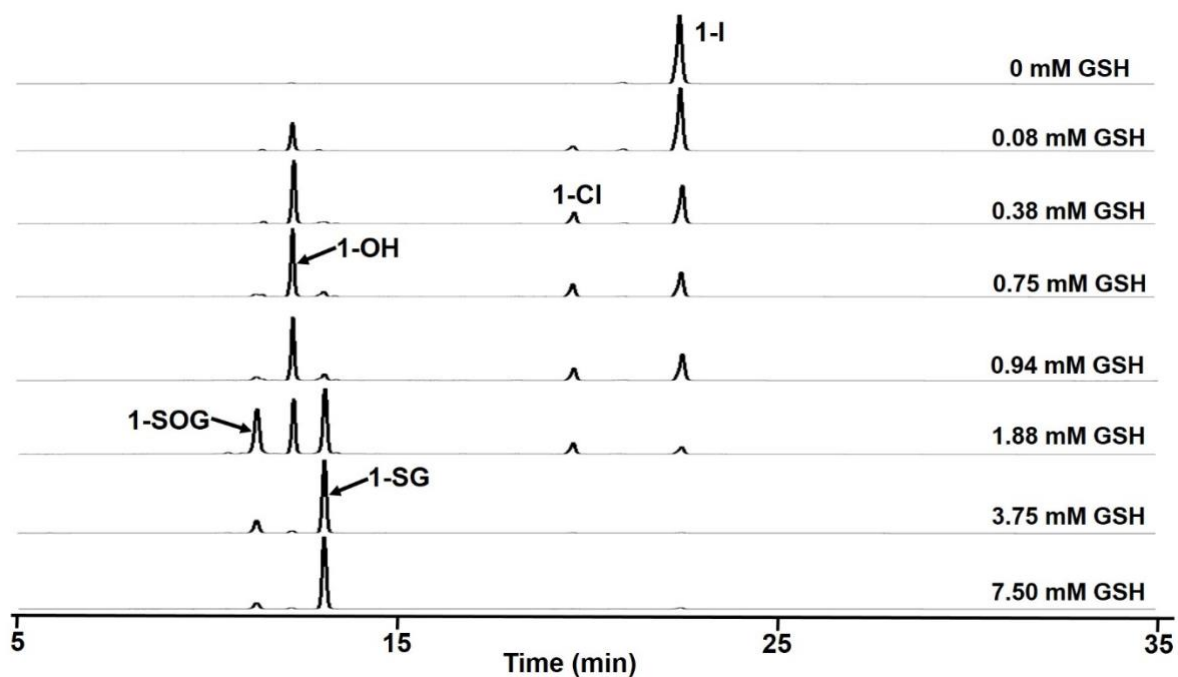


Fig. S21. HPLC separation for complex **1-I** (75 μ M) on incubation with various concentrations of GSH (0 - 7.5 mM) for 24 h at 310 K in phosphate buffer (75 mM, pH 7.40) and NaCl (25 mM). The solvent gradient used can be found in page S11.

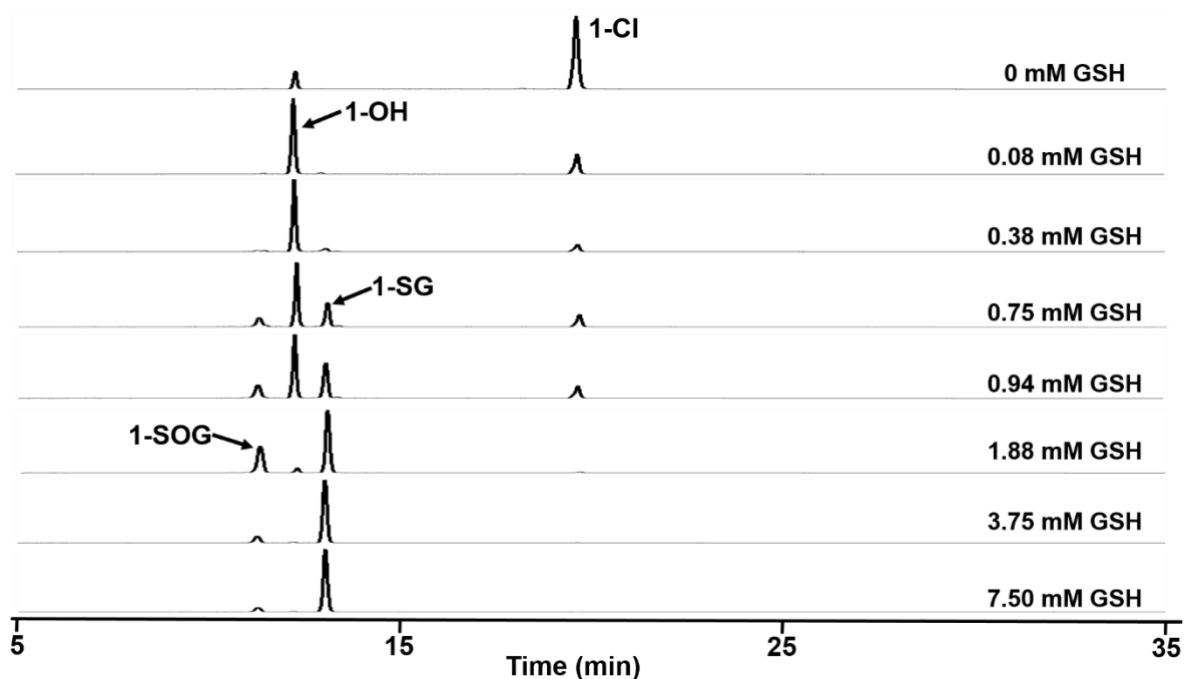


Fig. S22. HPLC separation of complex **1-Cl** (75 μ M) after incubation with various concentrations of GSH (0 - 7.5 mM) for 24 h at 310 K in phosphate buffer (75 mM, pH 7.40) and NaCl (25 mM). The solvent gradient used can be found in page S11.

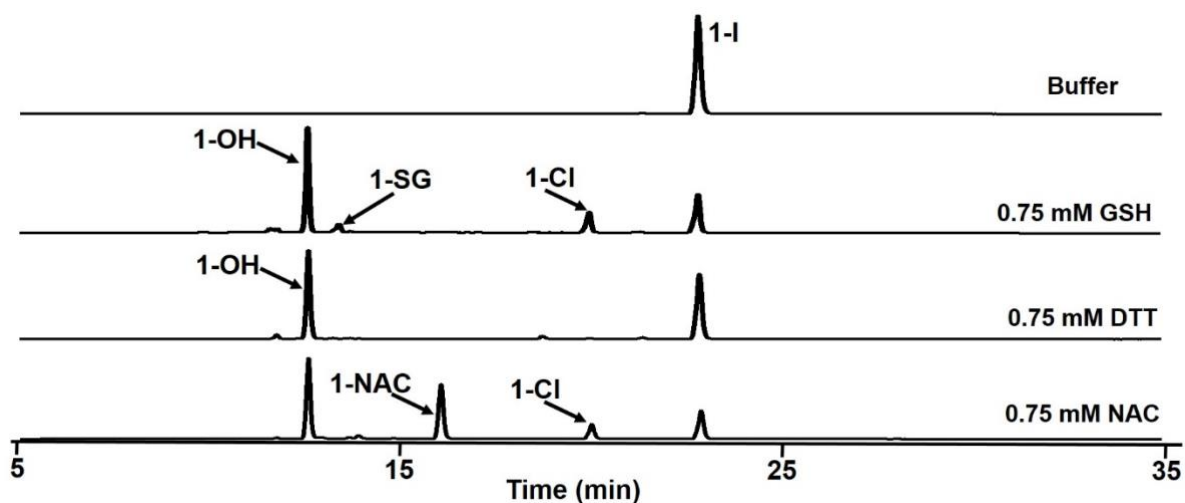


Fig. S23. HPLC separation of products from reactions of complexes **1-I** (75 μ M) with GSH, NAC or DTT (0.75 mM; 10 mol equiv) in 25 mM NaCl and 75 mM phosphate buffer (pH 7.40) at 310 K for 24h. The solvent gradient used can be found in page S11.

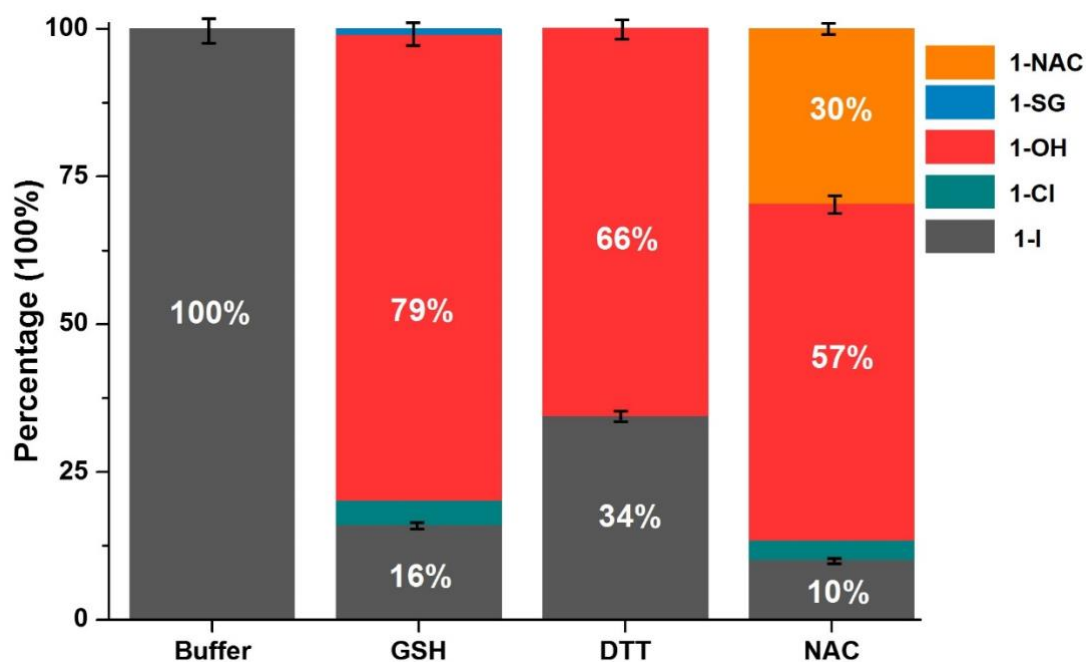


Fig. S24. Percentage (%) of osmium species (1-I, 1-Cl, 1-OH, 1-SG and 1-NAC) observed using HPLC (the solvent gradient used can be found in page S11) after reactions of 1-I (75 μ M) with thiols GSH, NAC or DTT (0.75 mM; 10 mol equiv) in 25 mM NaCl and 75 mM phosphate buffer (pH 7.40) at 310 K for 24h.

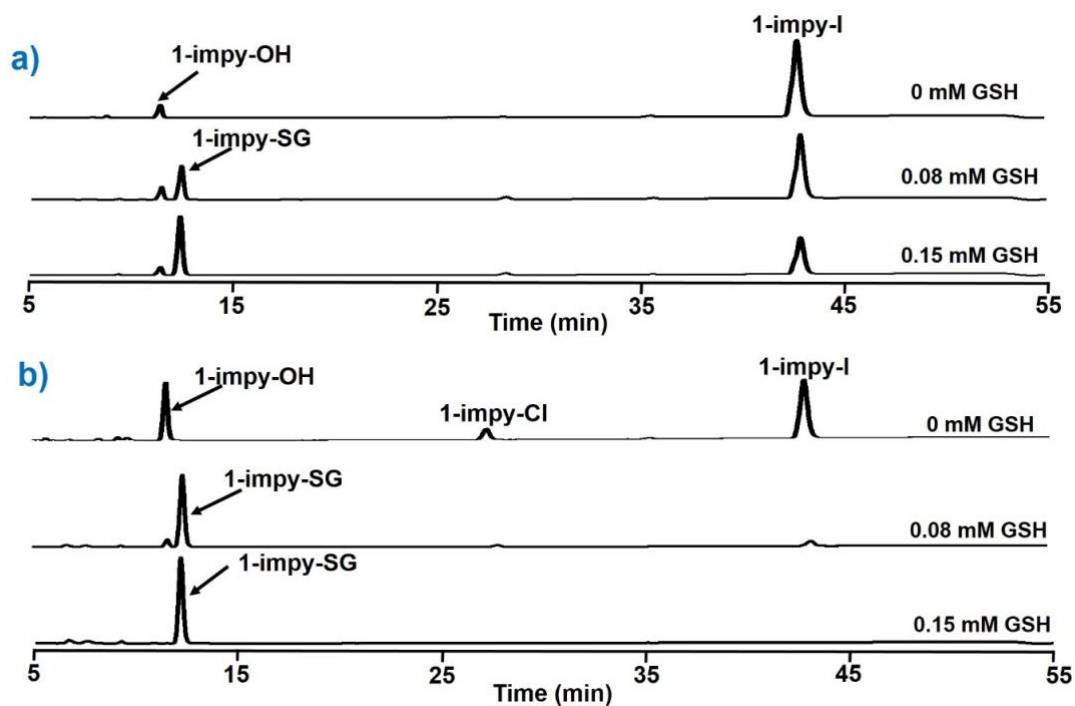


Fig. S25. HPLC separation of products from reactions of complex 1-imp-y-I (75 μ M) with 0 mM, 0.08 mM and 0.15 mM GSH for (a) 3 h and (b) 24 h at 310 K in phosphate buffer (75 mM, pH 7.40) and NaCl (25 mM). The solvent gradient used can be found in page S11.

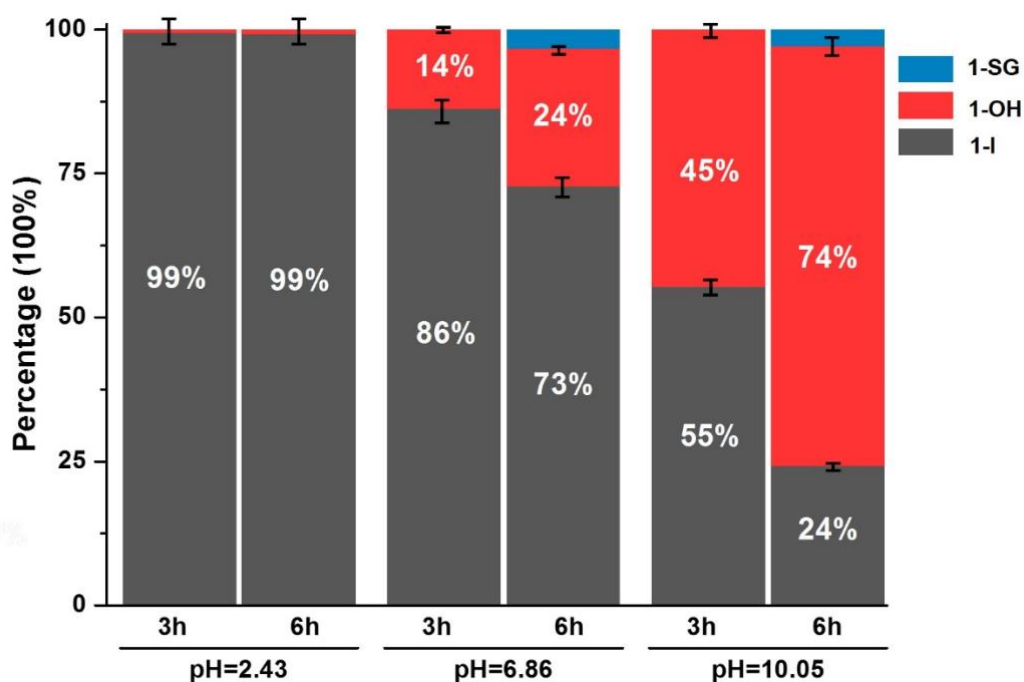


Fig.S26. Percentage of **1-OH**, **1-I** and **1-SG** species observed using HPLC (the solvent gradient used can be found in page S11) after reactions of **1-I** (100 μM) with GSH (200 μM ; 2 mol equiv) for 3 h and 6 h at 310 K at various pH values (pH=2.43, 6.86 and 10.05).

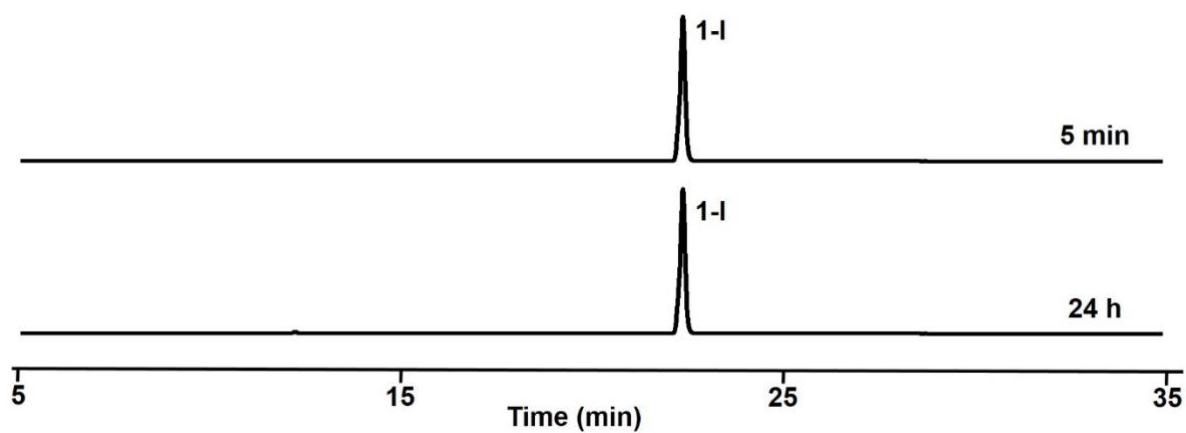


Fig. S27. HPLC for a solution of complex **1-I** (100 μM) after incubation at 310 K for 5 min or 24 h in high pH phosphate buffer (75 mM, pH 10.05). The solvent gradient used can be found in page S11.

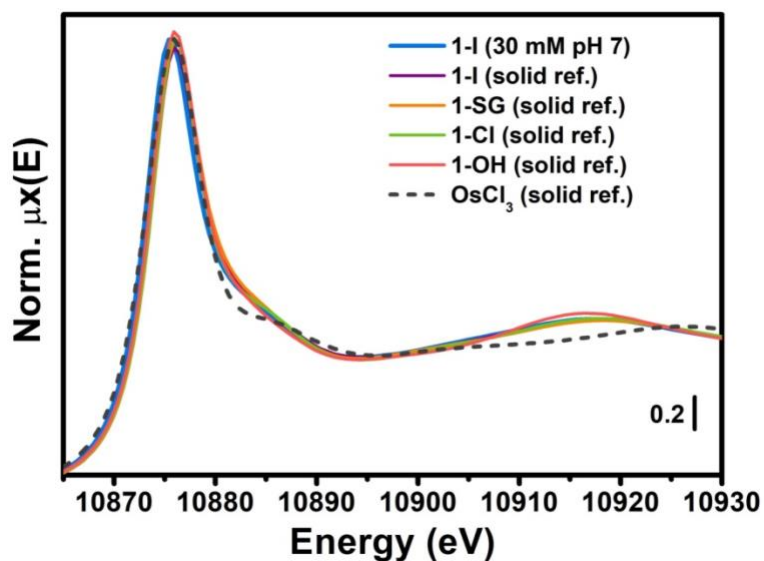


Fig. S28. Os L_3 -edge XANES spectra of **1-I** in the solution phase (30 mM, pH 7) compared to spectra of relevant reference compounds measured in the solid state, **1-I**, **1-SG**, **1-Cl**, **1-OH** and OsCl_3 .

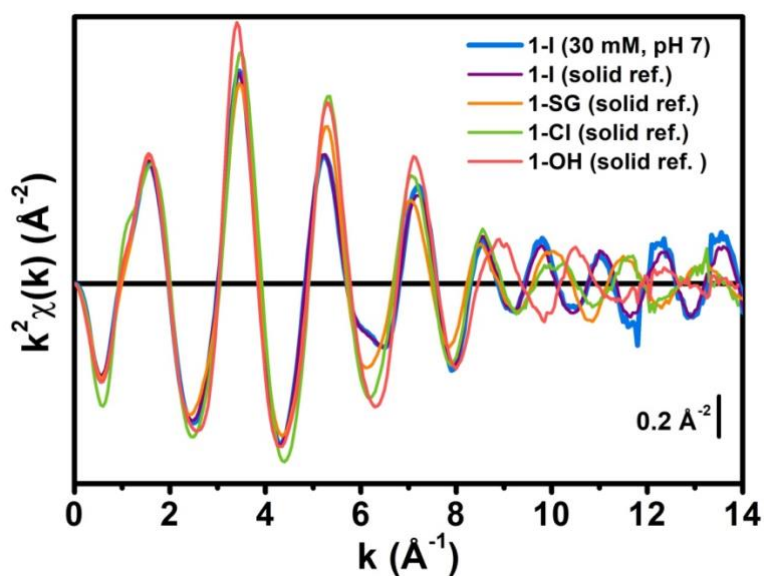


Fig. S29. Os L_3 -edge k_2 -weighted $k_2\chi(k)$ EXAFS spectra of **1-I** in the solution phase (30 mM, pH 7) compared to spectra of relevant reference compounds measured in the solid state, **1-I**, **1-SG**, **1-Cl**, and **1-OH**.

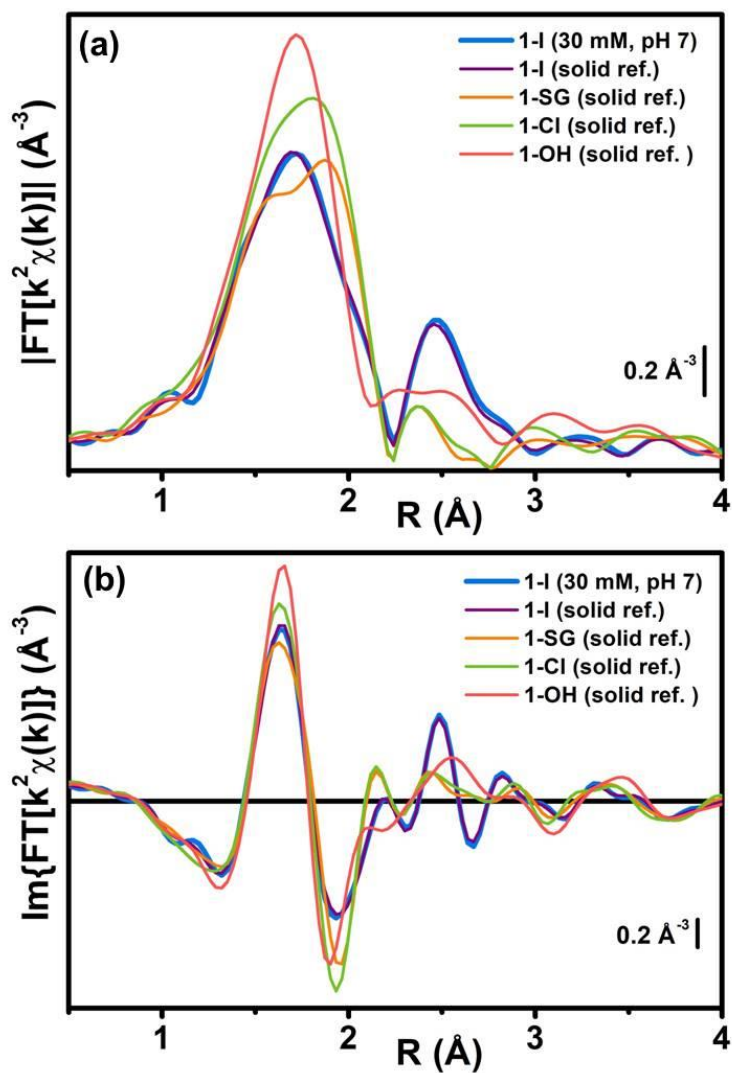


Fig. S30. Phase-uncorrected (a) magnitude and (b) imaginary part of the Fourier transformed (FT-) EXAFS functions in Fig.S29. The $k_2\chi(k)$ EXAFS functions here have been transformed in the (2.0-12.5) \AA^{-1} range for better comparison with *in situ* EXAFS spectra.

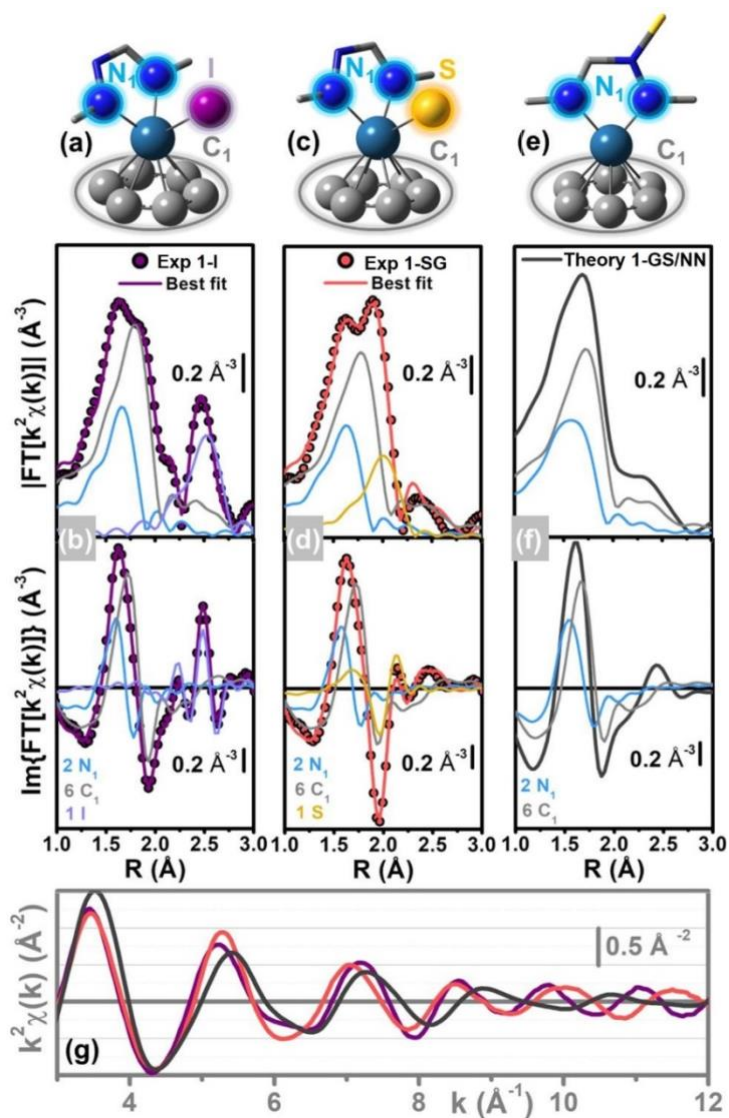


Fig.S31. Structural refinement from static EXAFS. (a, c, e) DFT-optimised structural models of the first coordination sphere of Os in (a) **1-I**, (c) **1-SG** and (e) **1-GS/NN** intermediate predicted by theory. Atom colour code: Os, indigo; N, blue; C, grey; S, yellow; I, purple. Coloured halos and corresponding labels denote the different sub-shells of scattering atoms employed for EXAFS fitting and simulation. (b, d) Comparison between experimental and best fit FT-EXAFS spectra (magnitude and imaginary part in top and bottom panels, respectively) for the solid-state references (b) **1-I** and (d) **1-SG** using the DFT models in parts (a) and (c), respectively, as initial input in the EXAFS fit. (f) Simulated EXAFS spectrum of the **1-GS/NN** intermediate, obtained based on the DFT-optimised geometry in part (e) by exploiting the results of the EXAFS fits shown in parts (b, d) on reference compounds **1-I** and **1-SG**. Parts (b, d, f) also show the principal contributions to the EXAFS signal, with the same colour code used to identify the different sub-shells of scattering atoms in parts (a, c, e). (g) Comparison between the experimental $k_2\chi(k)$ functions of the **1-I** (purple) and **1-SG** (red) solid-state references and the simulated $k_2\chi(k)$ for the **1-GS/NN** intermediate (dark grey). The spectra are shown in the (3.0-12.0) \AA^{-1} k-space range, which were also employed for the analysis in situ of the reaction between **1-I** and GSH using EXAFS

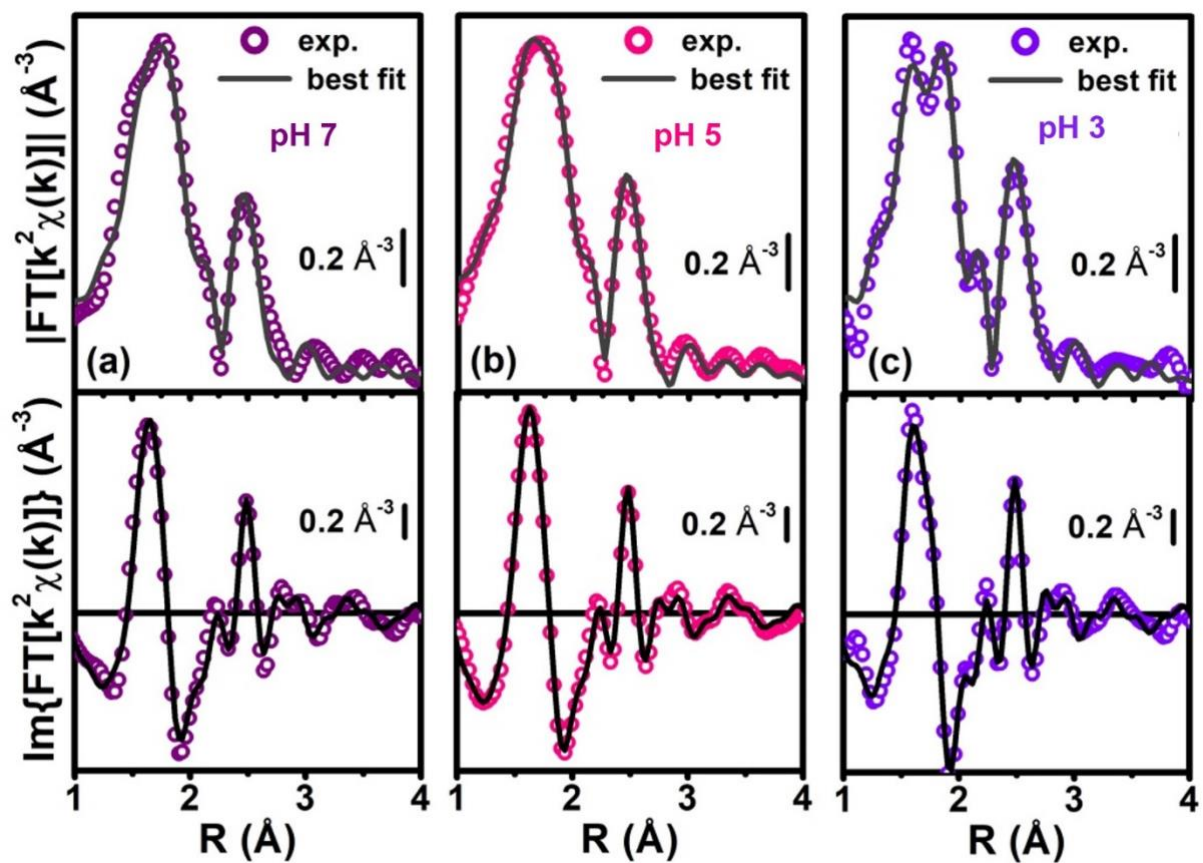


Fig. S32. Comparison between experimental (colored circles) and best fit (dark grey solid lines) FT-EXAFS spectra for 30 mM buffer solution of 1-I at (a) pH 7, (b) pH 5 and (c) pH 3, using the DFT models as initial input in the EXAFS fit (see Table S8 for quantitative results of the fits). Magnitude and imaginary parts of the FT are shown in top and bottom panels, respectively.

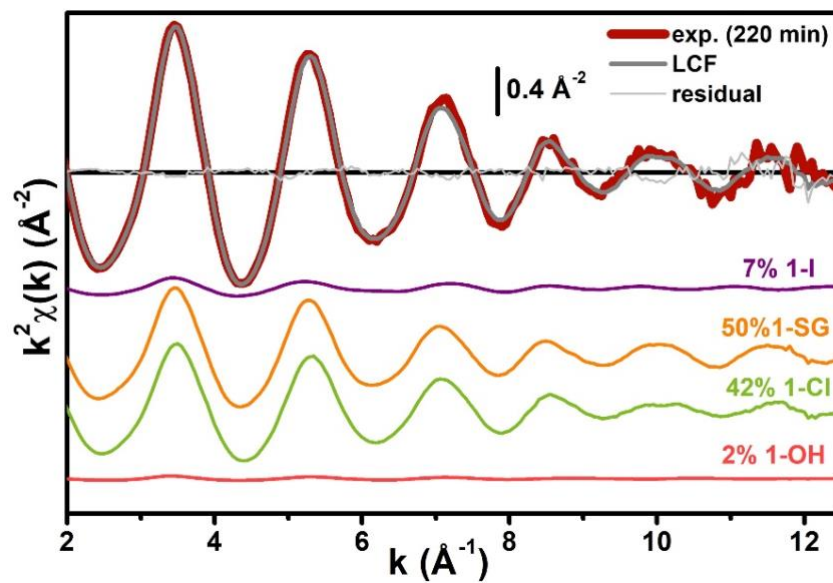


Fig. S33. Comparison between experimental *in situ* EXAFS spectrum (thick dark red line) collected after 220 min of reaction between **1-I** and GSH in a 30 mM buffer solution at pH 7, Os : GSH = 1:2 and the corresponding best fit curve (grey line), from LCF analysis in k-space. The scaled LCF contributions to the EXAFS signal related to **1-I**, **1-SG**, **1-CI** and **1-OH** are also shown, vertically translated for the sake of clarity.

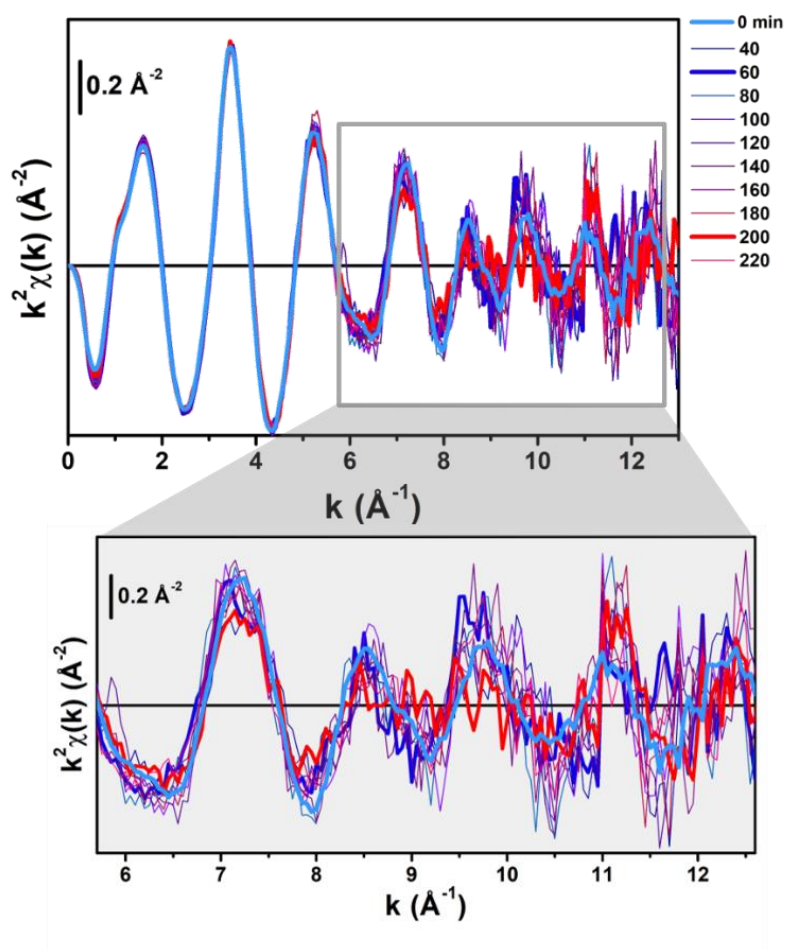


Fig. S34. Time-resolved *in situ* $k^2\chi(k)$ EXAFS spectra collected during reaction between 1-I and GSH in a 30 mM buffer solution at pH 5, Os : GSH = 2:1, transformed in the (2.0-12.5) \AA^{-1} range to obtain the FT-EXAFS spectra reported in Fig. 3c in the main text. The high- k region, where the biggest modifications as a function of the reaction time are observed, is highlighted by a grey box and magnified in the bottom inset.

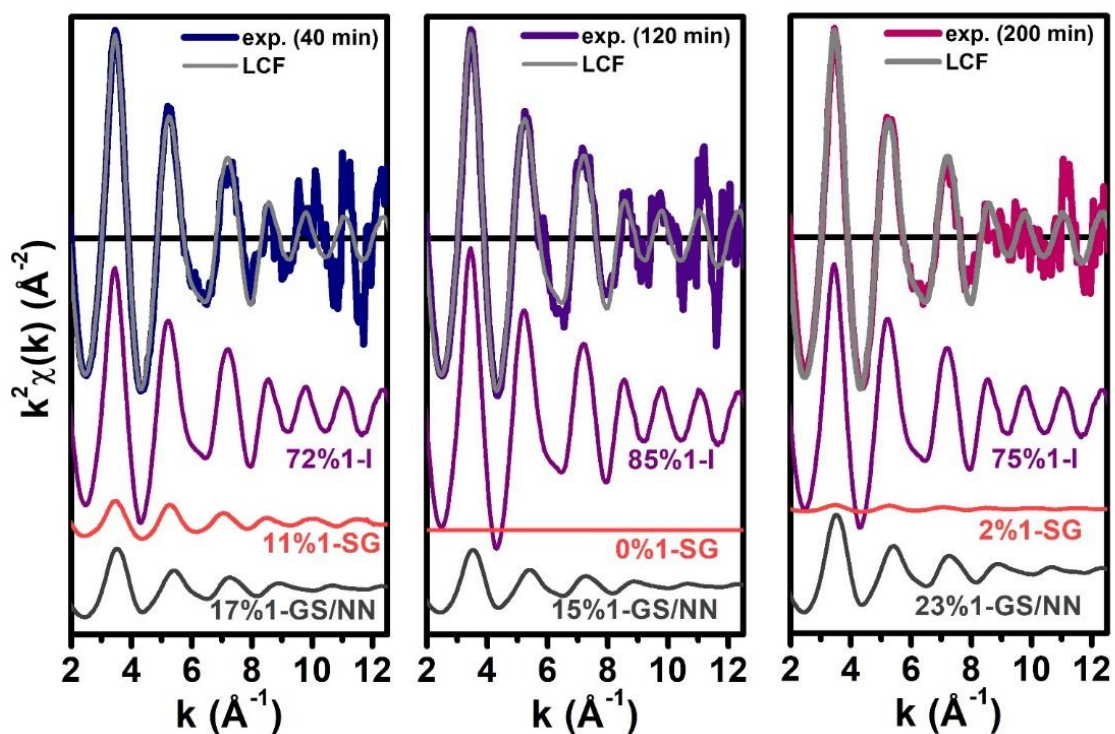


Fig. S35. Comparison between experimental *in situ* EXAFS spectra (thick coloured lines) collected during reaction between **1-I** and GSH in a 30 mM buffer solution at pH 5, O_s : GSH = 2:1 at selected reaction times and the corresponding best fit curves (grey lines), from LCF analysis in k -space. The three selected reaction times – 40 min (left panel), 120 min (middle panel), and 200 min (right panel), show the higher concentration of the **1-GS/NN** intermediate in the reaction mixture. The scaled LCF contributions to the EXAFS signal related to **1-I**, **1-SG** and **1-GS/NN** are also shown.

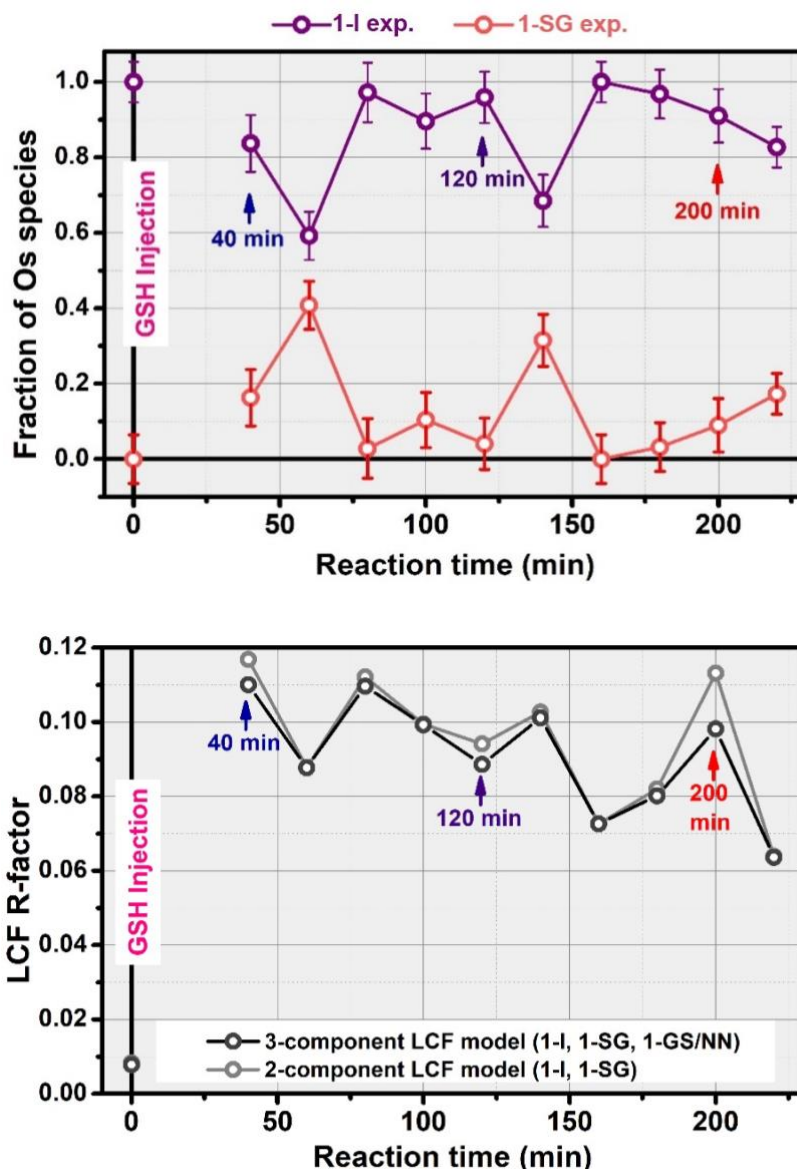


Fig. S36. Top panel: Results of LCF analysis of the time-resolved $k_2\chi(k)$ spectra collected during reaction between **1-I** and GSH in a 30 mM buffer solution at pH 5, Os : GSH = 2:1 (Fig. 3c, main text), using a two-component model (reactant **1-I** and product **1-SG**, without including the theoretical intermediate **1-GS/NN**). Bottom panel: comparison between the LCF R-factors obtained at each time point for the three-component model (reactant **1-I**; product **1-SG**, intermediate **1-GS/NN**: LCF results are shown in Fig. 3d, main text) and for the two-component model in the top panel. The coloured arrows highlight the reaction times corresponding to the concentrations of **1-GS/NN** (in the 16-24% total Os range), corresponding to systematic improvement of the LCF quality (lower R-factor values) for the three-component model.

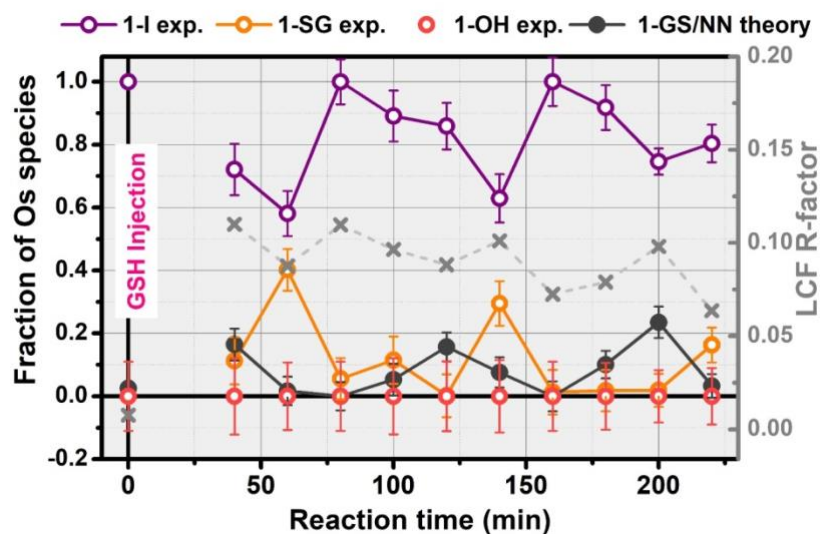


Fig. S37. Results from test LCF analysis of the time-resolved $k_2\chi(k)$ curves during reaction between **1-I** and GSH in a 30 mM buffer solution at pH 5, Os : GSH = 2:1, with inclusion in the fitting model also of the **1-OH** model compound together with **1-I**, **1-SG**, and the theoretical intermediate **1-GS/NN** (three-component model adopted in the main text, Fig. 3d). The LCF R-factors (grey \times) are also shown (right ordinated axis). The fraction of **1-OH** is optimized at (0.0 ± 0.1) over the whole investigated reaction time range, demonstrating that the **1-OH** species is not detectable under XAS experimental conditions. The LCF results are thus unaltered with respect to those in Fig. 3d, obtained using the three-component model.

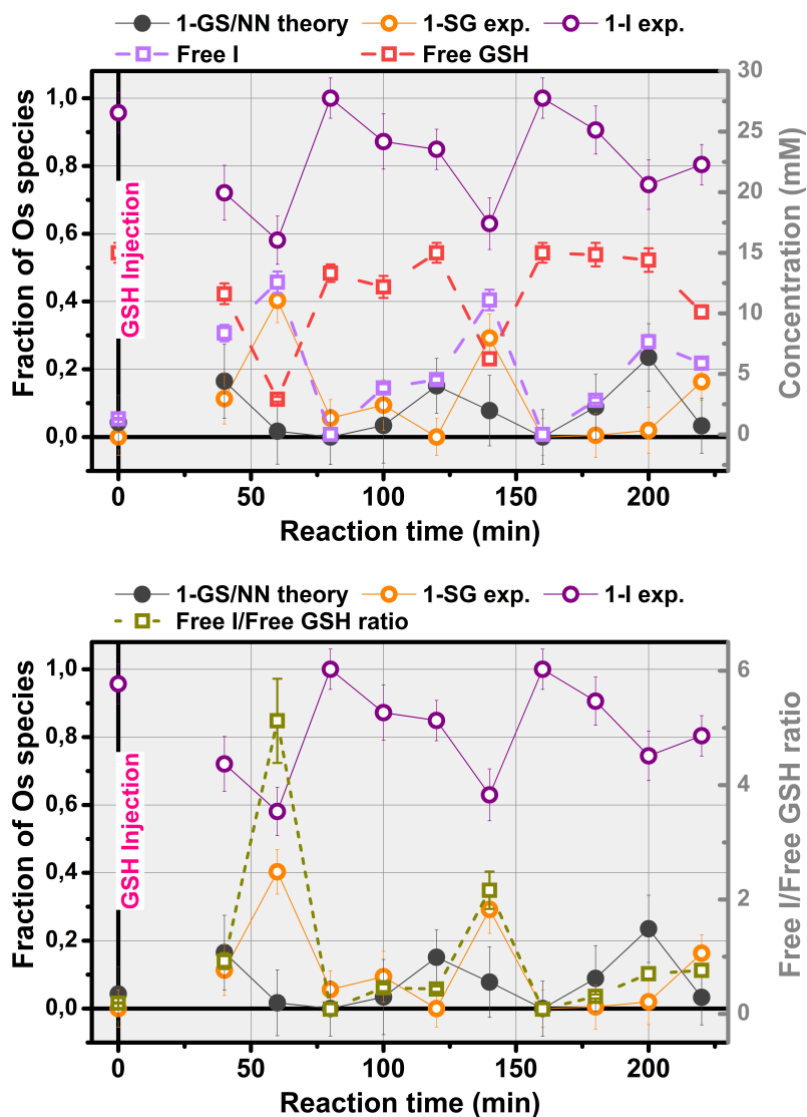


Fig. S38. Top panel: Comparison between the quantities of free I- ions and free GSH in the reaction environment with results of LCF analysis of the time-resolved $k_2\chi(k)$ spectra collected during reaction between **1-I** and GSH in a 30 mM buffer solution at pH 5, Os : GSH = 2:1, using a three-component model (reactant **1-I** and product **1-SG**, and theoretical intermediate **1-GS/NN**). Bottom panel: Comparison between the ratio of free I- ions/free GSH in the reaction environment with results of LCF analysis of the time-resolved $k_2\chi(k)$ spectra collected during reaction between **1-I** and GSH in a 30 mM buffer solution at pH 5, Os : GSH = 2:1, using a three-component model (reactant **1-I** and product **1-SG**, and theoretical intermediate **1-GS/NN**).

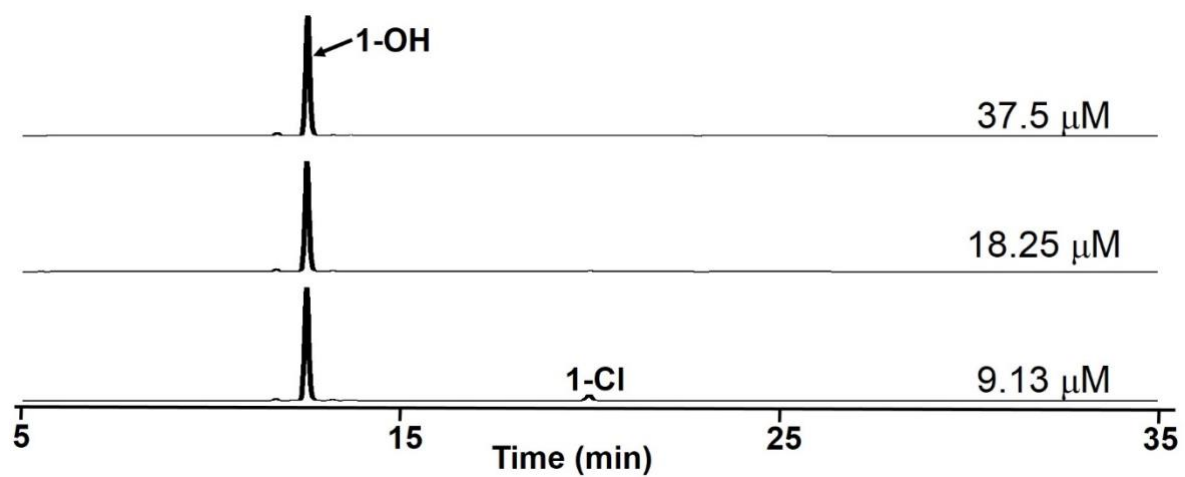


Fig. S39. HPLC separation of products from reactions of complex **1-CI** (75 μM) with 37.5 μM, 18.25 μM or 9.13 μM of GSH (0.5, 0.25 or 0.125 mol equiv) in 75 mM phosphate buffer (pH 7.4) at 310 K for 12 h.

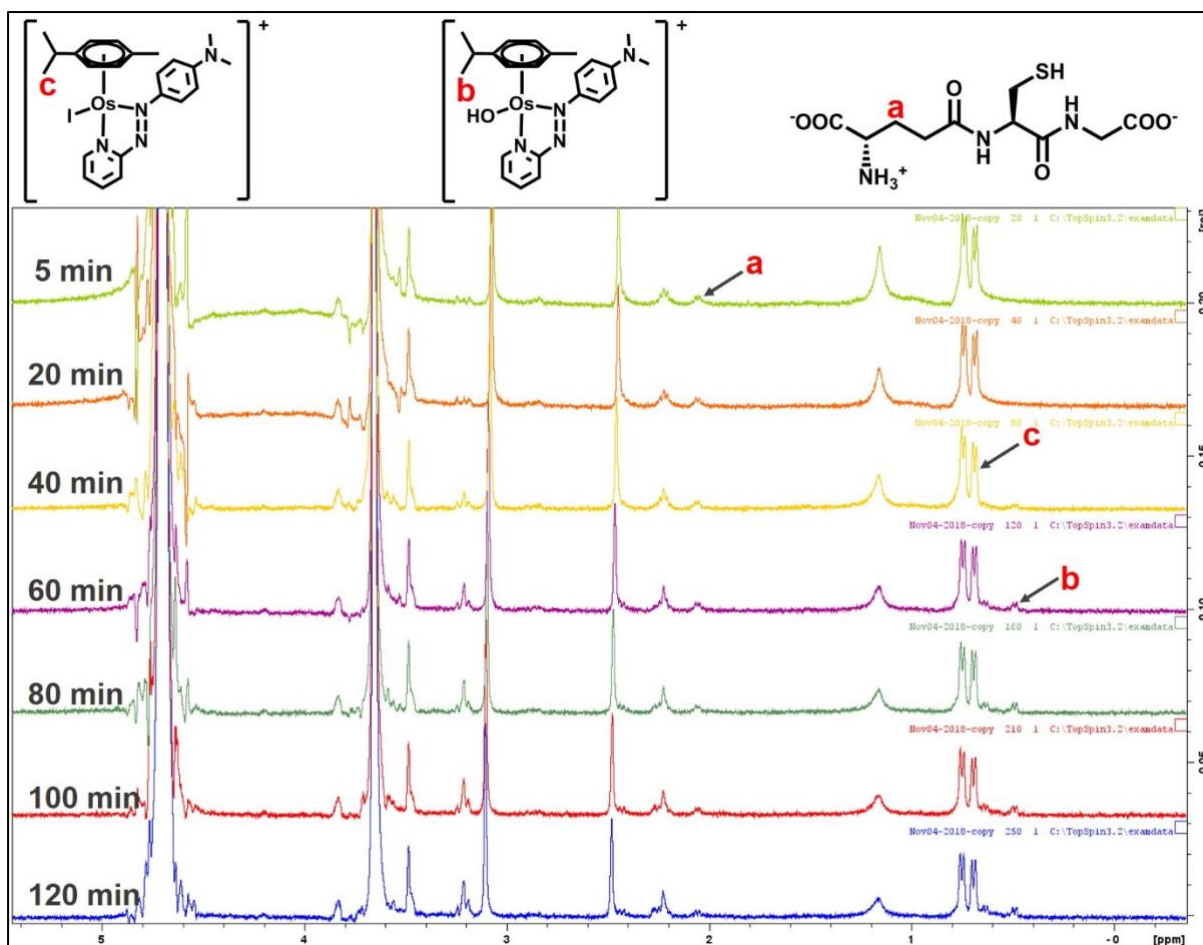


Fig. S40. ^1H NMR spectra and selected peak assignments for the reactions of **1-I** (2 mM) with GSH (200 μM , 10% mole equiv) in phosphate buffer (75 mM, pH 7.40) under N_2 after various reaction times at 298 K.

References

1. R. J. Needham, C. Sanchez-Cano, X. Zhang, I. Romero-Canelón, A. Habtemariam, M. S. Cooper, L. Meszaros, G. J. Clarkson, P. J. Blower and P. J. Sadler, *Angew. Chem. Int. Ed.*, 2017, **56**, 1017.
2. Y. Fu, A. Habtemariam, A. M. Pizarro, S. H. van Rijt, D. J. Healey, P. A. Cooper, S. D. Shnyder, G. J. Clarkson and P. J. Sadler, *J. Med. Chem.*, 2010, **53**, 8192.
3. Y. Fu, A. Habtemariam, A. M. B. H. Basri, D. Braddick, G. J. Clarkson and P. J. Sadler, *Dalton Trans.*, 2011, **40**, 10553.
4. Y. Fu, M. J. Romero, A. Habtemariam, M. E. Snowden, L. Song, G. J. Clarkson, B. Qamar, A. M. Pizarro, P. R. Unwin and P. J. Sadler, *Chem. Sci.*, 2012, **3**, 2485.
5. A. Krężel and W. Bal, *J. Inorg. Biochem.*, 2004, **98**, 161.
6. H. E. Gottlieb, V. Kotlyar and A. Nudelman, *J. Org. Chem.*, 1997, **62**, 7512.
7. O. Mathon, A. Beteva, J. Borrel, D. Bugnazet, S. Gatla, R. Hino, I. Kantor, T. Mairs, M. Munoz and S. Pasternak, *J. Synchrotron Radiat.*, 2015, **22**, 1548.
8. B. Ravel and M. Newville, *J. Synchrotron Radiat.*, 2005, **12**, 537.
9. L. Salassa, E. Borfecchia, T. Ruiu, C. Garino, D. Gianolio, R. Gobetto, P. J. Sadler, M. Cammarata, M. Wulff and C. Lamberti, *Inorg. Chem.*, 2010, **49**, 11240.
10. E. Borfecchia, K. A. Lomachenko, F. Giordanino, H. Falsig, P. Beato, A. V. Soldatov, S. Bordiga and C. Lamberti, *Chem. Sci.*, 2015, **6**, 548.
11. M. J. Frisch, G. W. Trucks, H. B. Schlegel, G. E. Scuseria, M. Robb, J. R. Cheeseman, G. Scalmani, V. Barone, B. Mennucci, G. A. Petersson, H. Nakatsuji, M. Caricato, X. Li, H. P. Hratchian, A. F. Izmaylov, J. Bloino, G. Zheng, J. L. Sonnenberg, M. Hada, M. Ehara, K. Toyota, R. Fukuda, J. Hasegawa, M. Ishida, T. Nakajima, Y. Honda, O. Kitao, H. Nakai, T. Vreven, J. A. Montgomery, P. Jr, J.E. , F. Ogliaro, M. Bearpark, J. J. Heyd, B. E., K. N.

- Kudin, V. N. Staroverov, R. Kobayashi, J. Normand, K. Raghavachari, A. Rendell, J. C. Burant, S. S. Iyengar, J. Tomasi, M. Cossi, N. Rega, J. M. Millam, M. Klene, J. E. Knox, J. B. Cross, V. Bakken, C. Adamo, J. Jaramillo, R. Gomperts, R. E. Stratmann, O. Yazyev, A. J. Austin, R. Cammi, C. Pomelli, J. W. Ochterski, R. L. Martin, K. Morokuma, V. G. Zakrzewski, G. A. Voth, P. Salvador, J. J. Dannenberg, S. Dapprich, A. D. Daniels, O. Farkas, J. B. Foresman, J. V. Ortiz, J. Cioslowski and D. J. Fox, *Gaussian 09, Revision C.01*, Gaussian, Inc.: Wallingford, CT, 2009.
12. A. D. Becke, *J. Chem. Phys.*, 1993, **98**, 5648.
 13. C. Lee, W. Yang and R. G. Parr, *Phys. Rev. B*, 1988, **37**, 785.
 14. S. Grimme, J. Antony, S. Ehrlich and H. Krieg, *J. Chem. Phys.*, 2010, **132**, 154104.
 15. T. H. Dunning and P. J. Hay, in *Modern theoretical chemistry*, Plenum Press, New York, NY, 1977, vol. 3, p. 1.
 16. K. Fukui, *J. Phys. Chem.*, 1970, **74**, 4161.
 17. C. Gonzalez and H. B. Schlegel, *J. Chem. Phys.*, 1989, **90**, 2154.
 18. S. Miertuš, E. Scrocco and J. Tomasi, *Chem. Phys.*, 1981, **55**, 117.
 19. J.-L. Pascual-Ahuir, E. Silla and I. Tunon, *J. Comput. Chem.*, 1994, **15**, 1127.
 20. D. A. McQuarrie and J. D. Simon, *Molecular Thermodynamics. University Science Books, Sausalito, CA*, 1999, 581.
 21. R. W. Ashcraft, S. Raman and W. H. Green, *J. Phys. Chem. B*, 2007, **111**, 11968.